



Mosaic composition of RIP1-RIP3 signalling hub and its role in regulating cell death

Xin Chen¹✉, Rongfeng Zhu¹, Jinjin Zhong², Yongfa Ying², Wenxin Wang¹, Yating Cao¹, Hanyi Cai¹, Xiang Li², Jianwei Shuai^{2,3} and Jiahui Han^{1,3,4}✉

RIP1 and RIP3, cell death mediators, form fibrous amyloids. How RIP1/RIP3 amyloidal oligomers assemble functional necrosomes and control cell death is largely unknown. Here we use super-resolution microscopy to directly visualize cellular necrosomes as mosaics of RIP1 and RIP3 oligomers. The small (initial) mosaic complexes are round, and the large mosaics are in a rod shape. RIP3 oligomers with sizes of tetramer or above are the domains in mosaics that allow MLKL, recruited by phosphorylated RIP3, to oligomerize for necroptosis. Unexpectedly, RIP1 autophosphorylation not only controls the ordered oligomerization of RIP1 but also is required for RIP1-initiated RIP3 homo-oligomerization in correct organization, which is indispensable for the formation of functional rod-shaped mosaics. Similarly, apoptosis initiated by enzymatically defective RIP3 requires the formation of rod-shaped mosaics of RIP3 and RIP1 oligomers. The revealing of nanoscale architecture of necrosomes here innovates our understanding of the structural and organizational basis of this signalling hub in cell death.

Necroptosis is a form of programmed cell death involved in the pathogenesis of inflammatory and degenerative diseases¹. The signalling pathway controlling tumour necrosis factor (TNF)-induced necroptosis has been defined: receptor-interacting protein (RIP) 1 dissociated from TNF receptor 1 (TNFR1) can recruit cytosolic Fas-associated death domain (FADD) and caspase-8 to form a pro-apoptotic complex II^{2,3}. Under the condition of caspase-8 inactivation, interaction between RIP1 and RIP3 could lead to the formation of necrosome and subsequent necroptosis^{4–7}. Effector protein mixed lineage kinase domain-like (MLKL) is recruited and phosphorylated by activated RIP3 in necrosome^{8,9}, and then translocates to the plasma membrane to induce cell lytic death^{10–13}. In this process, autophosphorylation of RIP1 is required for TNF-induced necroptosis^{14–17}. RIP1 does not directly phosphorylate RIP3¹⁸, but the interaction between RIP1 and RIP3 is required for signalling to RIP3 and subsequent necroptosis. RIP3 autophosphorylation at Ser227 (Thr231/Ser232 for mouse RIP3) is known to be essential for MLKL recruitment^{8,19}. After being phosphorylated by RIP3, MLKL is believed to unleash auto-inhibition, leading to oligomer formation and subsequent cell necroptosis^{20,21}.

When RIP3 kinase activity is diminished by mutations or treatment of kinase inhibitors, cell death could switch from necroptosis to apoptosis in cells and *in vivo*^{22,23}. Mouse harbouring RIP3 kinase-dead mutant (mRIP3-K51A) is viable, but another kinase-dead mutant of RIP3, mRIP3-D161N, causes spontaneous mouse death, indicating that these two RIP3 mutants have different kinase activity-independent functions²². The structure of RIP1–RIP3 interaction should play a role in this phenomenon, but its details are still largely unknown.

Cumulative evidence suggests that necrosome is a higher-order macromolecular complex. RIP1–RIP3 necrosome should have an amyloid feature in structure, as recombinant RIP homology-interacting motif (RHIM) domain of RIP1 and/or RIP3 or immu-

noprecipitated RIP1–RIP3 complex from necroptotic cells showed filamentous structures with variable lengths *in vitro*²⁴. An NMR study revealed that RHIM domains preferentially form RIP1 and RIP3 hetero-complex with amyloid feature²⁵. The X-ray structures of RIP3- and MLKL-fragment dimer, and MLKL monomer, were solved^{26,27}. Unfortunately, the heterogeneous nature of amyloid complex may make the structural study of the whole necrosome with X-ray or cryogenic electron microscopy difficult. The currently available information is not sufficient to predict the whole structure of necrosome, and no information is available for the architecture of functional necrosomes in cells undergoing necroptosis.

Stochastic optical reconstruction microscopy (STORM) is a single-molecule-based super-resolution imaging technology²⁸. It allows the visualization of biological systems with an optical resolution of tens of nanometres (nm), a tenfold higher resolution than that of traditional confocal imaging^{29,30}. In this Article, taking advantage of integral microscopies with around nanometre resolutions, we show that the cellular necrosomes are heterogeneous mosaics that consist of RIP1 homo- and RIP3 homo-oligomer portions in round or rod shapes. The round mosaics are smaller than rods and are probably the initial complexes that can progress to rods when additional RIP3 or RIP1 is incorporated. MLKL oligomers are at the periphery of necrosomes. Autophosphorylation of RIP1 is required for RIP1 oligomer to be formed in a rod shape, which initiates RIP3 homo-oligomerization in proper order, eventually leading to the rod-shaped necrosome formation. More importantly, MLKL oligomerization, a key prerequisite for cell necroptosis, relies on the stoichiometry of RIP3 in necrosome. In addition, the reverse signalling of necrosome to apoptosis by RIP3 inhibitor treatment or kinase-dead RIP3 mutants requires RIP1–RIP3 mosaic complexes. Taken together, this structural study of cellular necrosome at nanoscale sheds new light on the mechanism behind the assembling and function of necrosome.

¹State Key Laboratory of Cellular Stress Biology, Innovation Center for Cell Biology, School of Life Sciences, Xiamen University, Xiamen, China. ²Department of Physics and Fujian Provincial Key Laboratory for Soft Functional Materials Research, Xiamen University, Xiamen, China. ³National Institute for Data Science in Health and Medicine, Xiamen, China. ⁴Research Unit of Cellular Stress of CAMS, Cancer Research Center of Xiamen University, Xiang'an Hospital of Xiamen University, School of Medicine, Xiamen University, Xiamen, China. ✉e-mail: xchen@xmu.edu.cn; jhan@xmu.edu.cn

Results

Rod-shaped RIP1–RIP3 complexes in necroptotic cells. To analyse the structure of necrosome in cells, we reconstituted *MLKL*-knockout (KO) HeLa cell with *MLKL*-Flag(human *MLKL*) and also ectopically expressed HA-RIP3 (human RIP3) in this cell line. Necroptosis induction by TNF plus Smac mimetic plus zVAD (TSZ) led to the time-dependent formation of puncta with co-localized RIP1, RIP3 and MLKL (Extended Data Fig. 1). We then applied super-resolution microscopy (STORM) that provided ~12.93 nm lateral localization precision calculated by LAMA algorithm³¹, to map the nanoscale organization of necrosome (CF 647, Extended Data Fig. 2a). In unstimulated cells, RIP1 was visualized as dispersed small puncta, which probably represent free RIP1 in the cytosol of cells (TSZ 0 h, Fig. 1a). Upon TSZ addition, RIP1 forms larger punctate structures in round or rod shapes (TSZ 2 h or 4 h, Fig. 1a). RIP3 puncta exhibited similar shapes as RIP1 puncta except that more and larger rod-shaped structures were detected after long-time (4 h) TSZ treatment (Fig. 1b).

We further analysed our STORM images by machine-learning-based segmentation workflow³², and categorized necrosome puncta by their shapes (Extended Data Fig. 2b). Quantification of clusters showed that most of the RIP1 signals in unstimulated cells exhibited as dispersed small clusters with an average effective diameter of below 80 nm and an ellipticity of less than 2.00 (Extended Data Fig. 2c–e). More rods (ellipticity >2.00) were detected by RIP3 staining than were detected by RIP1 staining, especially at the late timepoint (4 h) of TSZ treatment (52.99% versus 24.36%, Fig. 1c). This could be due to more RIP3 being recruited to the complexes to form rods following TSZ treatment, making the rods detectable by RIP3 staining. Indeed, many more bigger RIP3-stained rods (length >400 nm, width >140 nm) were detected at the late timepoint (4 h) of TSZ treatment, but there was no such notable difference between early and late timepoints of TSZ treatment in RIP1-stained rods (Fig. 1d–g). We also did the same analysis by using antibodies against endogenous RIP1 and RIP3 in necroptotic HT-29 cells (Extended Data Fig. 3a). Similarly, more rods were detected by RIP3 staining than by RIP1 staining in the late-stage necroptotic HT-29 cells (25.67% versus 18.56%, Extended Data Fig. 3b,c). Long rods (>400 nm) were detected by RIP3 staining at the late timepoint (8 h) of TSZ treatment (Extended Data Fig. 3d–g). The above analysis indicated that the rods were extended by incorporation of additional RIP3 and/or RIP1 during the process of necroptosis and that RIP3 contributes more than RIP1 to the length of rod structures.

It needs to be noted that the above values are not the real parameter of RIP1–RIP3 complexes, as antibodies used in STORM imaging usually expand the size of an object by about 30 nm³³. To further evaluate the rod-shaped feature of the complex, we isolated RIP3 complexes in necroptotic cells via immunoprecipitation and visualized them by negative-stain electron microscopy (EM) or atomic force microscopy (AFM). The rod-shaped complex detected by EM exhibited a similar pattern as what we observed by STORM imaging in necroptotic cells (Fig. 1h). The width of the rods is about 40–50 nm, consistent with the value obtained by STORM after the influence of antibodies was taken into account. Furthermore, a ~30 nm unit-like organization was observed in the rod-shaped complex by EM (Fig. 1h) and AFM (Fig. 1i,j), suggesting a helical structure. Our data expand on previous results²⁴ and conclude that cellular RIP1–RIP3 complex has a round or rod shape with about 45 nm in diameter or width and hundreds of nanometres in length for the rods, and the rod-shaped complex probably has a helical structure.

Necrosomes are RIP1- and RIP3-oligomer mosaics. To reveal the nanoscale architecture of cellular necrosome, we first imaged RIP1–RIP3 complexes in HA-RIP3 and MLKL-Flag-expressing *MLKL*-KO HeLa cells by two-colour STORM, which provided an additional ~18.26 nm lateral localization precision with CF 568 (Extended Data

Fig. 4a). We confirmed that there is no crosstalk between CF 647 and CF 568 channels in our system (Extended Data Fig. 4b,c), and the workflow of segmentation/overlap analysis for two-colour STORM images works well (Extended Data Fig. 4d,e). Consistent with the single-colour images (Fig. 1a,b), TSZ treatment induced both round- and rod-shaped RIP1–RIP3 complexes and the proportion of rod complexes increased over time after the treatment (Fig. 2a), indicating that round RIP1–RIP3 complexes can proceed to rod-shaped complexes. In these cells, the RIP1–RIP3 nanoscale structures could be categorized into three types: type I structure is a small round RIP1 cluster with no co-localized RIP3; type II structure is a round mosaic with about equal amounts of RIP1 and RIP3 clusters; type III structure is a mosaic in rod shape containing comparable amounts of RIP1 and RIP3 clusters (IIIa) or more RIP3 clusters than RIP1 clusters (IIIb) (Fig. 2b). The total area of RIP3 to that of RIP1 in rods was significantly higher than that in round complexes, suggesting RIP3 homo-oligomer is the major contributor to rod-shaped mosaic complexes (Fig. 2c). We also analysed the respective widths of RIP1 and RIP3 portions in the rods and found they are both about 110 nm (Fig. 2d), consistent with our results obtained by single-colour STORM (Fig. 1d,e). RIP1 and RIP3 portions in the mosaics have variable sizes, but many of them are larger than RIP1 or RIP3 monomer in unstimulated cells (Fig. 2b, green or purple arrows, Fig. 2e,f and Extended Data Fig. 5a), indicating that the mosaics are mainly constituted by RIP1 and RIP3 homo-oligomers. Similar mosaics of RIP1 and RIP3 oligomers were found in several types of cells undergoing necroptosis (Extended Data Fig. 5b–e), indicating that mosaic is a general feature of cellular necrosome.

As the recruitment of MLKL to necrosome is crucial for necroptosis, we further determine whether the RIP1–RIP3 complexes contain MLKL by co-staining MLKL and RIP3 in HA-RIP3 and MLKL-Flag-expressing *MLKL*-KO HeLa cells. We observed round RIP3 structures with little co-localized MLKL (1) and RIP3 rods with different amounts of co-localized MLKL (2a and 2b) (Fig. 2g and Extended Data Fig. 5f). Quantitatively, the total area of MLKL to that of RIP3 in rod-shaped necrosomes is higher than that in round-shaped necrosomes (Fig. 2h). MLKL signals were frequently concentrated on the outside of RIP3 rods, suggesting MLKL is positioned on the surface of RIP1–RIP3 complex (Fig. 2i). Moreover, the MLKL clusters in the rod-shaped RIP3 necrosome were substantially larger than MLKL monomer in unstimulated cells (Fig. 2g, yellow arrow, Fig. 2j and Extended Data Fig. 5f), implying MLKL oligomerization occurs on the surface of necrosomes.

To determine whether the RIP1–RIP3 mosaics are functional necrosomes, we counterstained the necroptotic cells with antibodies against RIP3 and phospho-RIP3 (pRIP3) or phospho-MLKL (pMLKL). The signals of pRIP3 and pMLKL were validated as they were largely present in TSZ-treated HeLa cells expressing wild-type (WT) RIP3 but barely detectable in TSZ-treated HeLa cells expressing loss-of-function RIP3-S227A mutant (Fig. 2k,m). pRIP3/pMLKL puncta were much easier to be detected in rod-shaped than in rounded complexes (Fig. 2k,m, left), indicating rod-shaped complexes are functionally potent necrosomes. We note that the round-shaped complexes are also functional necrosomes as they can induce MLKL phosphorylation. Quantification analysis further revealed that the size of pRIP3 and pMLKL puncta in the necrosome rods was larger than that in round-shaped necrosome (Fig. 2l,n), indicating that those rod-shaped mosaics are probably the major contributors in initiating necroptosis. The data obtained by analysing TSZ-treated HT-29 WT, RIP3-KO and *MLKL*-KO cells with super-resolution imaging also confirmed that mosaics are functional necrosomes (Extended Data Fig. 5g–j).

RIP3 homo-oligomer is obligatory for MLKL oligomer formation. MLKL is recruited and phosphorylated by activated RIP3 in necrosome^{8,9}, and then translocates to the plasma membrane

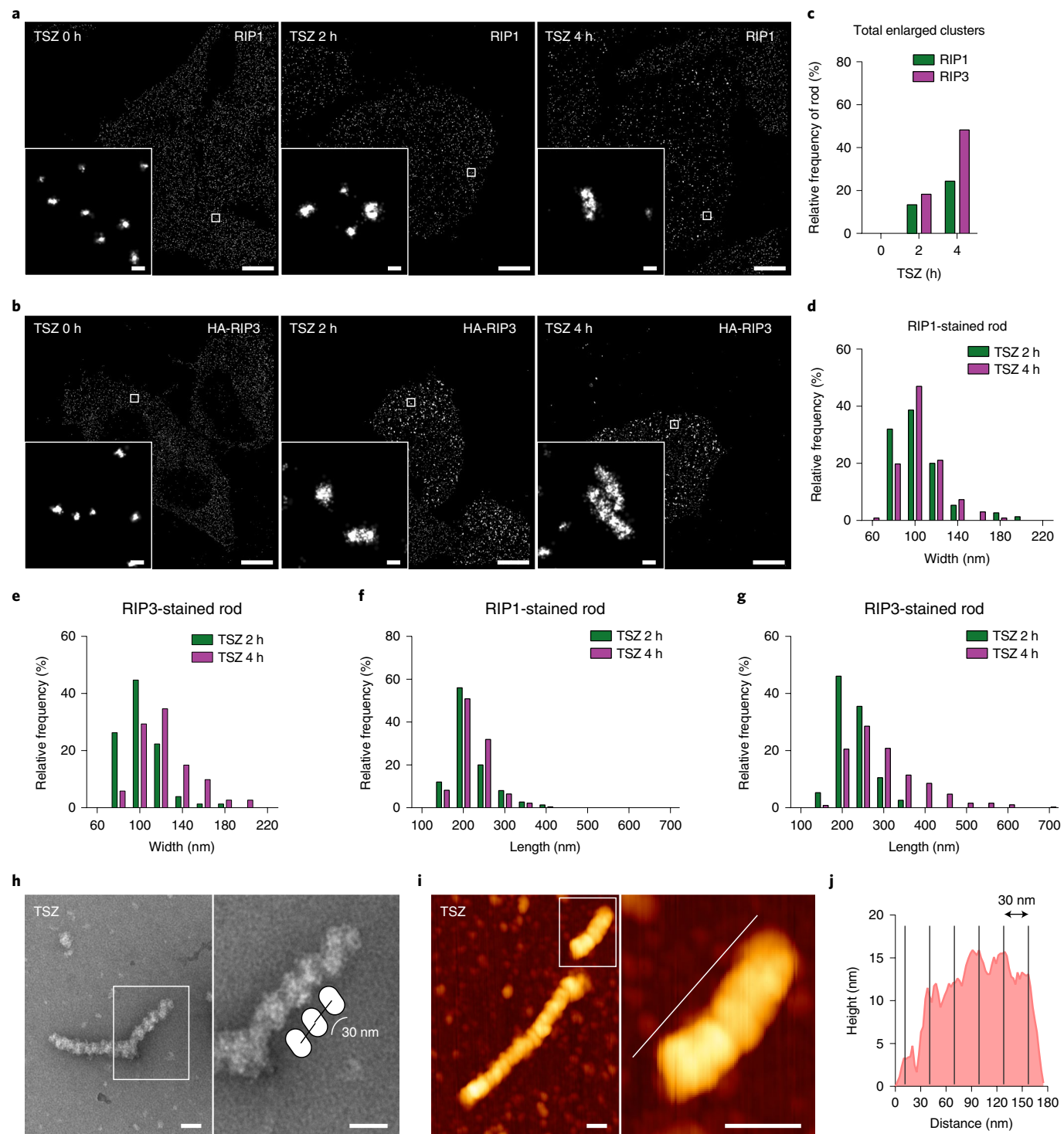


Fig. 1 | Nanoscale imaging analysis of necrosomes in necrototic cells. **a, b**, Single-colour STORM images of RIP1 (**a**) and RIP3 (**b**) in HA-RIP3-expressing HeLa cells treated with TSZ (T: TNF, 10 ng ml⁻¹; S: Smac mimetic (SM-164), 100 nM; Z: zVAD-fmk, 20 μM) for indicated time. Magnified images outlined by the white box are shown as inset figures, highlighting the RIP1 or RIP3 necrosome during cell necrosis. **c**, Percentage of rod-shaped structures detected by RIP1 or RIP3 staining in total enlarged clusters (RIP1, $n=16, 560$ and 952 for TSZ 0, 2 and 4 h, respectively; RIP3, $n=36, 417$ and 777 for TSZ 0, 2 and 4 h, respectively) by TSZ stimulation. The definitions of TSZ-induced cluster as round- or rod-shaped structure are described in Extended Data Fig. 2d,e. **d–g**, Width (**d**) and length (**f**) distributions of rods detected by RIP1 staining ($n=75$ and 232 for TSZ 2 and 4 h, respectively) or width (**e**) and length (**g**) distributions of RIP3-stained rods ($n=76$ and 375 for TSZ 2 and 4 h, respectively) in necrototic HeLa cells treated as in **a**. In **c–g**, n refers to the number of structures analysed across three independent experiments. **h–j**, Flag-RIP3-expressing HeLa cells were treated with TSZ for 4 h. The RIP3-containing complex was immunoprecipitated with an anti-Flag antibody and visualized by using negative-stain EM (**h**) or AFM (**i**). Representative images of rod-shaped RIP3 from five independent EM experiments and two independent AFM experiments are shown. The distance between repeated units outlined by white boxes is about 30 nm (magnified image, **h**). Intensity profile along the white line in **i** (grey lines are 30 nm apart, **j**). Scale bars, 5 μm (original images in **a** and **b**), 100 nm (magnified images in **a** and **b**) and 50 nm (**h, i**). Statistical source data are provided in Source Data Fig. 1. Also see Extended Data Figs. 1–3.

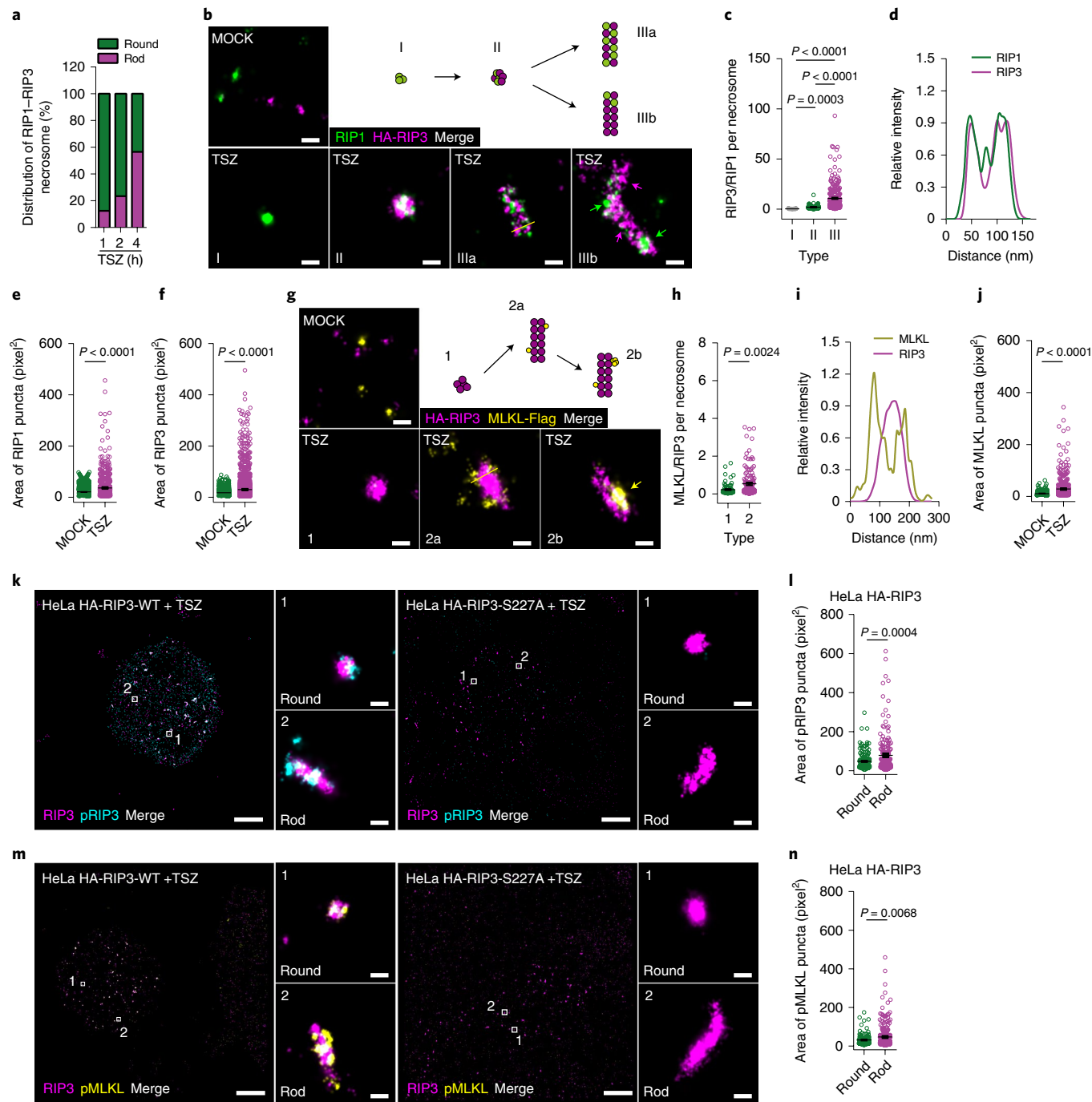


Fig. 2 | RIP1-RIP3 mosaics are functional necrosomes. **a**, Distribution of round-/rod-shaped RIP1-RIP3 complexes in HA-RIP3 and MLKL-Flag-reconstituted MLKL-KO HeLa cells at different timepoints of TSZ treatment ($n=112, 137$ and 173 structures analysed across three independent experiments for TSZ 1, 2 and 4 h, respectively). **b**, Two-colour STORM images showing RIP1-RIP3 localizations in the cells from **a** treated with dimethyl sulfoxide (DMSO; MOCK) or TSZ. Schematic illustrations are provided to categorize the necrosomes observed into different types (I-III). Green and purple arrows show RIP1 and RIP3 oligomer in a rod-shaped necrosome, respectively. **c**, The ratio of total area of RIP3 to that of RIP1 in each type of complex ($n=27, 112$ and 285 structures for type I, II and III, respectively). **d**, Intensity profiles of RIP1 and RIP3 along a yellow line in IIIa of **b**. **e,f**, Area distribution of RIP1 ($n=2,398$ and 680 structures for MOCK and TSZ, respectively; **e**) or RIP3 ($n=2,642$ and $2,720$ structures for MOCK and TSZ, respectively; **f**) puncta in **b**. **g**, Two-colour STORM images showing RIP3-MLKL localizations in cells from **a** treated with DMSO or TSZ. Schematic illustrations are provided to categorize the necrosomes observed into different types (1 and 2). Yellow arrow shows MLKL oligomer in a rod-shaped necrosome. **h**, The ratio of total area of MLKL to that of RIP3 in type I ($n=88$ structures) and II ($n=171$ structures) complexes. **i**, Intensity profiles of RIP3 and MLKL along a yellow line in 2a of **g**. **j**, Area distribution of MLKL puncta ($n=3,085$ and 538 structures for MOCK and TSZ, respectively) in **g**. **k-n**, Two-colour STORM images showing the localizations of pRIP3 (**k**) or pMLKL (**m**) and RIP3 in TSZ-treated HeLa cells expressing RIP3-WT or RIP3-S227A mutant. Area of pRIP3 ($n=160$ and 179 structures for round and rod, respectively; **l**) and pMLKL ($n=119$ and 280 structures for round and rod, respectively; **n**) puncta in round-/rod-shaped necrosome was calculated. STORM images in **b**, **g**, **k** and **m** are representative of three independent experiments. Data in **c,e,f,h,j,l** and **n** are mean \pm s.e.m. and pooled from three independent experiments. All P values are determined by two-tailed, unpaired t -test, except in **c**, where they are determined by Kruskal-Wallis test with Dunn's multiple comparisons test. Scale bars, $5\mu\text{m}$ (original images in **k** and **m**) and 100 nm (**b**, **g** and magnified images in **k** and **m**). Statistical source data are provided in Source Data Fig. 2. Also see Extended Data Figs. 4 and 5.

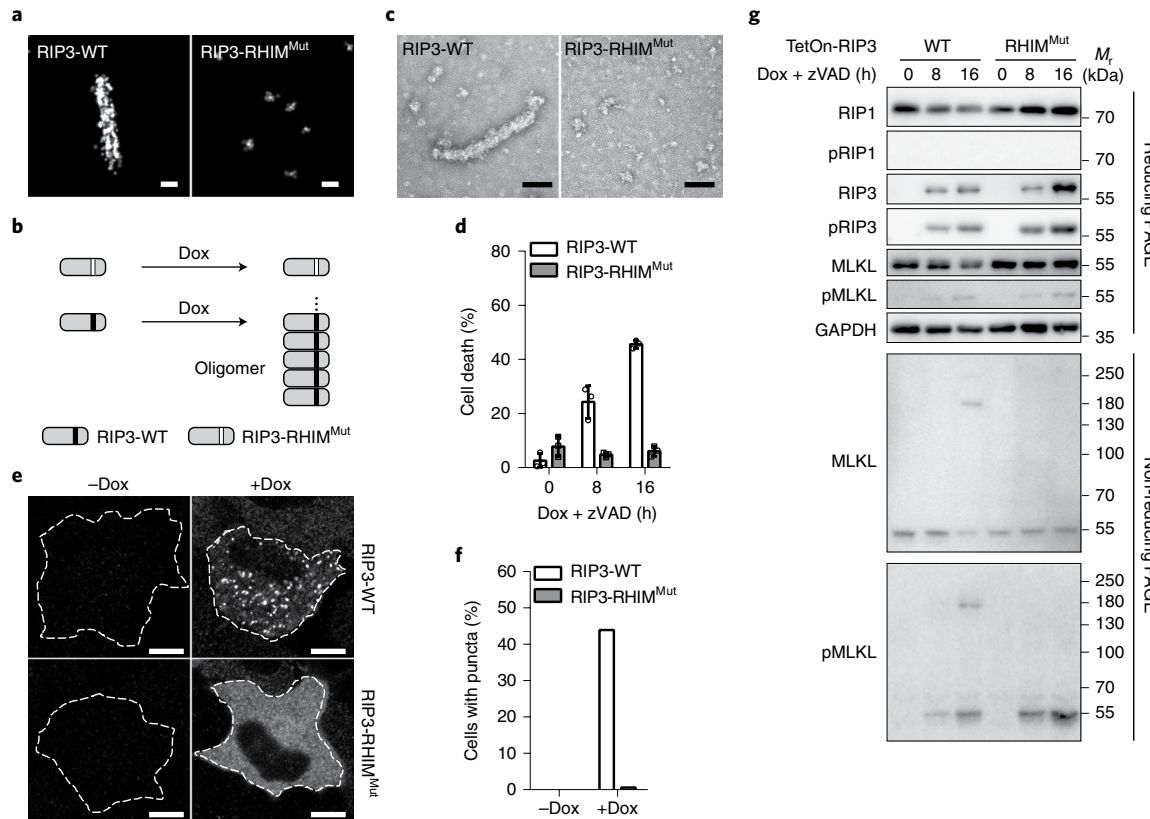


Fig. 3 | RHIM-dependent RIP3 oligomerization is required for MLKL oligomerization but dispensable for phosphorylation of RIP3 and MLKL.

a, Single-colour STORM images of RIP3 in Flag-RIP3-WT- or Flag-RIP3-RHIM^{mut}-expressing HeLa cells treated with TSZ. **b**, Schematic representation showing oligomerization of RIP3 via Dox-induced overexpression. **c–g**, Expression of Flag-RIP3-WT or Flag-RIP3-RHIM^{mut} was induced by Dox, and zVAD addition was included to inhibit the effect of caspases. The RIP3-containing complex was immunoprecipitated with an anti-Flag antibody and visualized by using negative-stain EM (**c**). Cell viability was measured on the basis of quantitation of the ATP present (**d**). Data are represented as mean \pm s.d. of biological triplicates. Confocal images of RIP3 are shown (**e**), and the fraction of cells with RIP3 puncta was calculated (**f**). $n=148-278$ cells pooled by two independent experiments. Cell lysates were collected and analysed by immunoblotting for the indicated proteins under reducing or non-reducing conditions (**g**). Scale bars, 10 μ m (**e**) and 100 nm (**a,c**). Unprocessed blots and statistical source data are provided in Source Data Fig. 3. Also see Extended Data Fig. 6.

to induce cell lytic death^{10–13}. But how MLKL oligomerization is regulated remains elusive. Since the mutation of RHIM sequence in RIP3 to tetra-alanine (RIP3-RHIM^{mut}) eliminated TSZ-induced rod-shaped necrosome (Fig. 3a), we employed doxycycline (Dox)-induced expression of RIP3-WT or RIP3-RHIM^{mut} in HeLa cells to obtain monomeric and oligomeric RIP3, respectively (Fig. 3b). zVAD was included in all experiments to prevent possible apoptosis. Overexpressed RIP3-WT but not RIP3-RHIM^{mut} exhibited RIP3 rod structure and resulted in necroptosis of HeLa cells (Fig. 3c,d). Confocal imaging further confirmed that RIP3 puncta initiated by RIP3 itself are only detected in HeLa cells expressing RIP3-WT but not RIP3-RHIM^{mut} (Fig. 3e,f). The RIP3 homo rods looked similar to RIP1-RIP3 mosaic rods in width and length by STORM imaging (Extended Data Fig. 6a). Surprisingly, RIP3-WT and RIP3-RHIM^{mut} produced roughly equal amounts of phosphorylated MLKL, suggesting that both Dox-induced RIP3-WT and RIP3-RHIM^{mut} can autophosphorylate to a certain extent and recruit/phosphorylate MLKL (Fig. 3g, upper panel). Interestingly, only overexpressed RIP3-WT but not RIP3-RHIM^{mut} can lead to MLKL oligomerization, as indicated by the detection of MLKL tetramer in non-reducing SDS-polyacrylamide gel electrophoresis (SDS-PAGE) (Fig. 3g, bottom panel). It is clear that phosphorylation of MLKL cannot cause MLKL oligomerization. Although the phosphorylation level of MLKL in RIP3-RHIM^{mut} cells was equal to

that in RIP3-WT cells, the RIP3-RHIM^{mut} cells exhibited no death (Fig. 3d), indicating that phosphorylated monomeric MLKL cannot trigger necroptosis. The same results were obtained by using HeLa RIP1-KO cells (Extended Data Fig. 6b–f), excluding possible involvement of RIP1. This result may explain the observation by Petrie et al. that phosphomimetic human MLKL mutants (T357E-S358E and T357E-S358D) did not gain function to cause cell death²¹. Thus, RHIM-dependent RIP3 homo-oligomerization is required for MLKL oligomerization but dispensable for RIP3 auto-phosphorylation and MLKL phosphorylation by RIP3. To trigger necroptosis, MLKL needs to be phosphorylated and oligomerized.

RIP3 oligomers with sizes of tetramer or above make MLKL oligomers. To further investigate the role of RIP3 homo-oligomer in MLKL activation, we directly manipulated the stoichiometry of RIP3 complex by using a protein–protein interaction system mediated by the FK506 binding protein (FKBP)/FKBP-rapamycin binding (FRB) domain of the mammalian target of rapamycin/FKBP-Phe36Val (FV)^{34–36}. In brief, FV-fused RIP3-WT and RIP3-RHIM^{mut} should assemble as oligomers and dimers upon AP20187 treatment, respectively (Fig. 4a). FRB-FKBP-fused RIP3-RHIM^{mut} should form tetramers in the presence of rapamycin³⁷. The plasmids expressing these proteins were individually introduced into RIP1-KO HeLa cells, and RIP3 dimer, tetramer

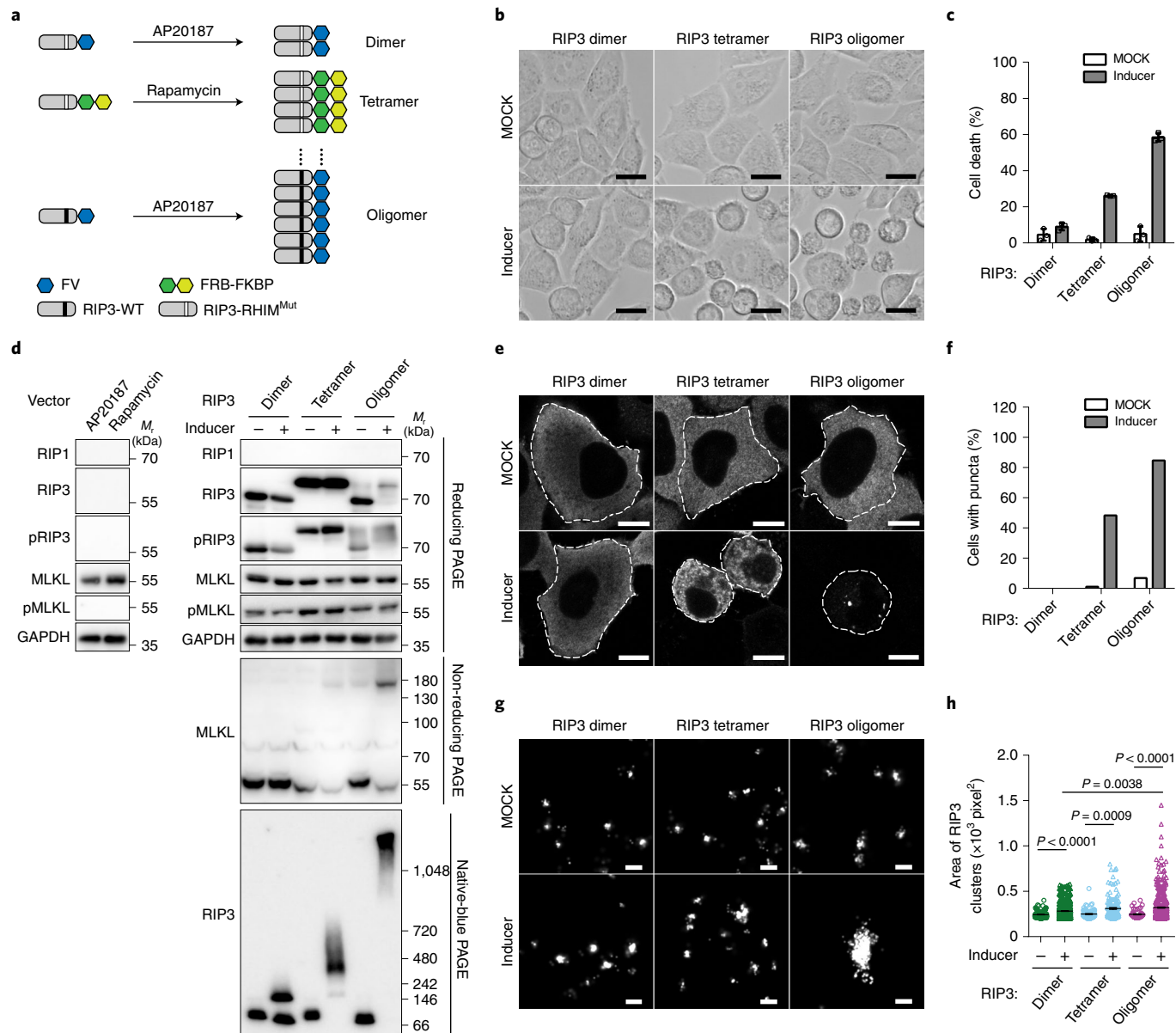


Fig. 4 | RIP3 oligomers with sizes of tetramer or above enable phosphorylated MLKL to form oligomers and subsequently trigger cell necroptosis.

a, Schematic representation showing dimerization, tetramerization or oligomerization of RIP3 by inducible FV or FRB-FKBP domain interaction. **b–c**, RIP1-deficient HeLa cells expressing different RIP3 fusion proteins as shown in **a** were treated with DMSO or corresponding inducer for 6 h. The morphologies of live and dead cells are shown (**b**), and the cell viability was measured on the basis of quantitation of the ATP present (**c**). Data are represented as mean \pm s.d. of biological triplicates. Cell lysates were collected and analysed by immunoblotting for the indicated proteins under denaturing, non-reducing or native conditions (**d**). Cells transduced with empty vector were used as a control. Confocal (**e**) or STORM (**g**) images of RIP3 in cells treated as in **b**. The fraction of cells harbouring puncta in **e** were determined (**f**). $n = 95$ –147 cells pooled by two independent experiments. Area distribution of RIP3 clusters in **g** was calculated (**h**). Data are mean \pm s.e.m. and pooled from three independent experiments ($n = 175$ structures for dimer + DMSO, $n = 618$ structures for dimer + inducer, $n = 82$ structures for tetramer + DMSO, $n = 135$ structures for tetramer + inducer, $n = 52$ structures for oligomer + DMSO and $n = 459$ structures for oligomer + inducer). P values are determined by Kruskal–Wallis test with Dunn's multiple comparisons test. Scale bars, 50 μ m (**b**), 10 μ m (**e**) and 100 nm (**g**). Unprocessed blots and statistical source data are provided in Source Data Fig. 4.

or oligomer was induced by corresponding inducers. While RIP3 dimer did not induce cell death, RIP3 tetramer or oligomer led to substantial cell death with necroptotic characteristics (Fig. 4b,c). Similar to the result in Dox-induced RIP3 overexpression experiments (Fig. 3g), phosphorylated MLKL was detected in cells where these fused RIP3 were expressed (Fig. 4d, upper panel). Notably, phosphorylation of MLKL alone is not sufficient to trigger necroptosis as it already appeared in the cells without oligomerization inducers (Fig. 4d, upper panel). As expected, only tetrameric or

oligomeric RIP3 induced MLKL oligomerization whereas MLKL in cells with dimeric RIP3 was still monomeric (Fig. 4d, middle panel). The induction of RIP3 dimer/tetramer/oligomer was confirmed by blue native PAGE (Fig. 4d, bottom panel). We also performed a microscopic study of these cells and found that only RIP3 tetramer/oligomer formed visible puncta (Fig. 4e,f). Super-resolution imaging further provided the size distribution of RIP3 complex in these cells (Fig. 4g,h). In conclusion, RIP3 homo-tetramer is the minimum size required to mediate MLKL oligomerization.

RIP1 autophosphorylation directs necrosomes in a rod shape. It is known that RIP1 kinase activity is required for TNF-induced necroptosis^{14–17}. Pretreatment of RIP1 kinase inhibitor Nec-1 inhibited TSZ-induced RIP1 phosphorylation, downstream RIP3 and MLKL phosphorylation in RIP3-expressing HeLa cells (Extended Data Fig. 7a) and necroptosis in RIP3-expressing HeLa, HT-29, LS 174T and THP-1 cells (Extended Data Fig. 7b–e), but not the co-localization of RIP1 and RIP3 (Fig. 5a,c) and Extended Data Fig. 7f,g). STORM imaging showed that RIP1–RIP3 were co-localized within the structures in irregular shapes in the presence of Nec-1 (Fig. 5a,c). The diameters of these RIP1–RIP3 structures were more than 200 nm, much bigger than the diameter or width of round- or rod-shaped necrosomes (Fig. 5a,c). These complexes are RIP1 and RIP3 mosaics but with disordered organization of RIP1/RIP3 clusters. They rarely progress to rod-like shapes in the presence of Nec-1 as the long side (length) of these RIP1–RIP3 complexes was significantly shorter than that in the cells without Nec-1 treatment (Fig. 5b). EM analysis of RIP1–RIP3 complex isolated from cells in the absence or presence of Nec-1 treatment confirmed the results obtained by super-resolution imaging (Fig. 5d,e). Therefore, Nec-1 impairs the formation process of round- and rod-shaped necrosomes, making the RIP1–RIP3 complexes become irregular in shape and disordered in organization.

To rule out the possibility that Nec-1 directly inhibits RIP3 homo-interaction, we overexpressed RIP3 in *RIP1*-KO HeLa cells and tested whether Nec-1 affects the formation of RIP3 self-assembled rods. Super-resolution imaging showed that Nec-1 did not influence the formation of RIP3 rods by overexpressed RIP3 (Fig. 5f,g).

We then sought to examine the rod formation of overexpressed RIP1 with or without Nec-1 treatment in RIP1-deficient HeLa cells. RIP1 kinase-dead mutants (K45A or D138N) or autophosphorylation site mutants (S161E or N) were also included³⁸ (Extended Data Fig. 7h). Nec-1 addition, kinase-dead mutations or autophosphorylation defect mutation all gave rise to sizes of RIP1 complexes that were represented as massive big/bright puncta, whereas the phosphomimetic mutant (S161E) behaved similarly to WT RIP1 (Extended Data Fig. 7i). Further visualization of these puncta by STORM reveals that overexpressed RIP1 formed rod-shaped structures (Fig. 5h,i). In contrast, RIP1 with its activity inhibited by Nec-1 or by kinase-dead mutations still formed complexes, but the complexes were enlarged and in irregular shapes. S161E mutation retained RIP1 at rod-shaped structure, whereas RIP1 harbouring S161N mutation was similar to kinase-dead mutants (Fig. 5h,j). Thus, RIP1 autophosphorylation controls its own oligomerization in proper order, and this proper organization of RIP1 oligomers appears to be required for the initiation of functional RIP3 oligomerization in the process of necosome formation.

RIP3 autophosphorylation is not linked to rod shape of necrosomes. Next, we also assessed the role of RIP3 autophosphorylation in the formation of rod-shaped structure. GSK'840 and dabrafenib (Dabra), two specific RIP3 kinase inhibitors^{23,39}, inhibited cell necroptosis and reduced phosphorylation of RIP3 but not the formation of RIP1–RIP3 co-localized puncta (Fig. 6a,b and Extended Data Fig. 8a,b). In addition, the length of RIP3-stained rods was not substantially affected by RIP3 inhibitors (Fig. 6c,d). Similarly, blocking RIP3 kinase activity prevented HT-29, LS 174T and THP-1 cells from undergoing TSZ/TNF plus cycloheximide plus zVAD (TCZ)-induced necroptosis but could not abolish the formation of rod-shaped RIP1–RIP3 structure in these cells (Fig. 6e–h). Moreover, RIP3 mutants defective in its kinase activity (D160N) or the recruitment of MLKL (S227A) were still able to form rod structures with similar lengths of WT RIP3 rods (Fig. 6i,j), even though RIP3 autophosphorylation and necroptosis were inhibited (Fig. 6k,l). In sharp contrast to RIP3-D160N, another RIP3 kinase-dead mutant (K50A) forms small puncta rather than rods, indicating

this mutation impairs RIP3 homo-interaction in a RIP3 kinase activity-independent manner (Fig. 6i,j). Since RIP3 formed rods when overexpressed, we tested the role of RIP3 autophosphorylation in this spontaneous RIP3 complex formation. Co-expressing the WT or enzyme-inactive form (R179G) of PPM1B, a RIP3 phosphatase that de-phosphorylated RIP3⁴⁰, did not alter overexpressed RIP3-induced puncta in human embryonic kidney (HEK) 293T cells (Extended Data Fig. 8c,d). STORM imaging further revealed that these RIP3 puncta were in a rod shape with similar lengths regardless of whether PPM1B-WT or PPM1B-R179G was co-expressed (Extended Data Fig. 8e,f). Taken together, our data demonstrate that autophosphorylation of RIP3 is not required for rod-shaped necosome formation, though it is required for recruiting and phosphorylating MLKL.

Apoptosis by RIP3 kinase inhibition relies on RIP3 oligomerization. It was reported that signalling to apoptosis can be initiated by RIP3 kinase inhibitor GSK'872 or D161N mutation that impaired murine RIP3 (mRIP3) kinase activity^{22,23}. However, K51A mutant of mRIP3, another kinase-inactive mutant, cannot cause spontaneous RIP1-dependent apoptosis in cells and mice^{22,23}. Ectopic expression of mRIP3-WT or mRIP3-D161N in RIP3-deficient L929 cells led to necroptosis or apoptosis, respectively, and in both cases the formation of mRIP1–mRIP3 co-localized rod-shaped puncta with the mosaic pattern was observed, whereas the expression of mRIP3-K51A did not lead to cell death as well as the formation of rod-shaped puncta (Fig. 7a–d). Interestingly, the addition of RIP3 kinase inhibitor GSK'872 resulted in apoptosis and the formation of mRIP1–mRIP3 co-localized rod with mosaic pattern in the cells expressing mRIP3-K51A (Fig. 7a–d), indicating GSK'872 can promote RIP3 to form rod-shaped complex and recruit RIP1. As expected, GSK'872 had no effect on mRIP3-D161N and inhibited mRIP3-WT-initiated necroptosis. mRIP3-RHIM^{Mut} was included as a negative control in these experiments. Similarly, the K50A but not D160N of human RIP3 is defective in the formation of rod-shaped structure (Fig. 6i,j). We obtained similar results in HEK293T cells (Extended Data Fig. 9). It appears that D161N mutation or GSK'872 endows RIP3 a special configuration that allows RIP3 to form ordered oligomers. This event can initiate RIP1 oligomerization possibly in a configuration that is favourable to recruit FADD and caspase-8 for apoptosis, and the loss of RIP3 kinase activity is either not required or not sufficient for RIP3 to trigger apoptosis. To further support the importance of organized rod structure, we tested the effect of amyloid-binding chemical Congo red (CR), which disrupts the organization of necosome and impairs cell necroptosis²⁴. The addition of CR substantially inhibited L929 cell apoptosis induced by GSK'872 treatment but did not disrupt the RIP1–RIP3 interaction, which is evident by the presence of RIP1–RIP3 co-localized puncta (Fig. 7e,f). CR treatment did not substantially alter the frequency of RIP1–RIP3 puncta in L929 cells (Fig. 7g), but it generated large disordered RIP3 complexes, which might impair the recruitment of other components for apoptosis (Fig. 7h). Thus, the specially organized mosaic of RIP1 and RIP3 is required for kinase-dead RIP3 or GSK'872 to trigger apoptosis via RIP1.

Discussion

This study uncovered that cellular necrosomes are mosaics composed of heterogeneous RIP1 and RIP3 oligomers (Figs. 1 and 2). The shape of functional necrosomes can be round or rod, and the rods are probably developed from the round necrosomes. By using energy-based molecular modelling in referencing published structural information of RIP1–RIP3 interaction^{25,26,41,42}, and on the basis of our integral microscopic data (Figs. 1 and 2), we proposed a hypothetic model of RIP1–RIP3 mosaics: RHIM-dependent RIP1/RIP3 homo- or hetero-interaction results in bidirectional β sheets (Extended Data Fig. 10a, (I)), which could further form helical

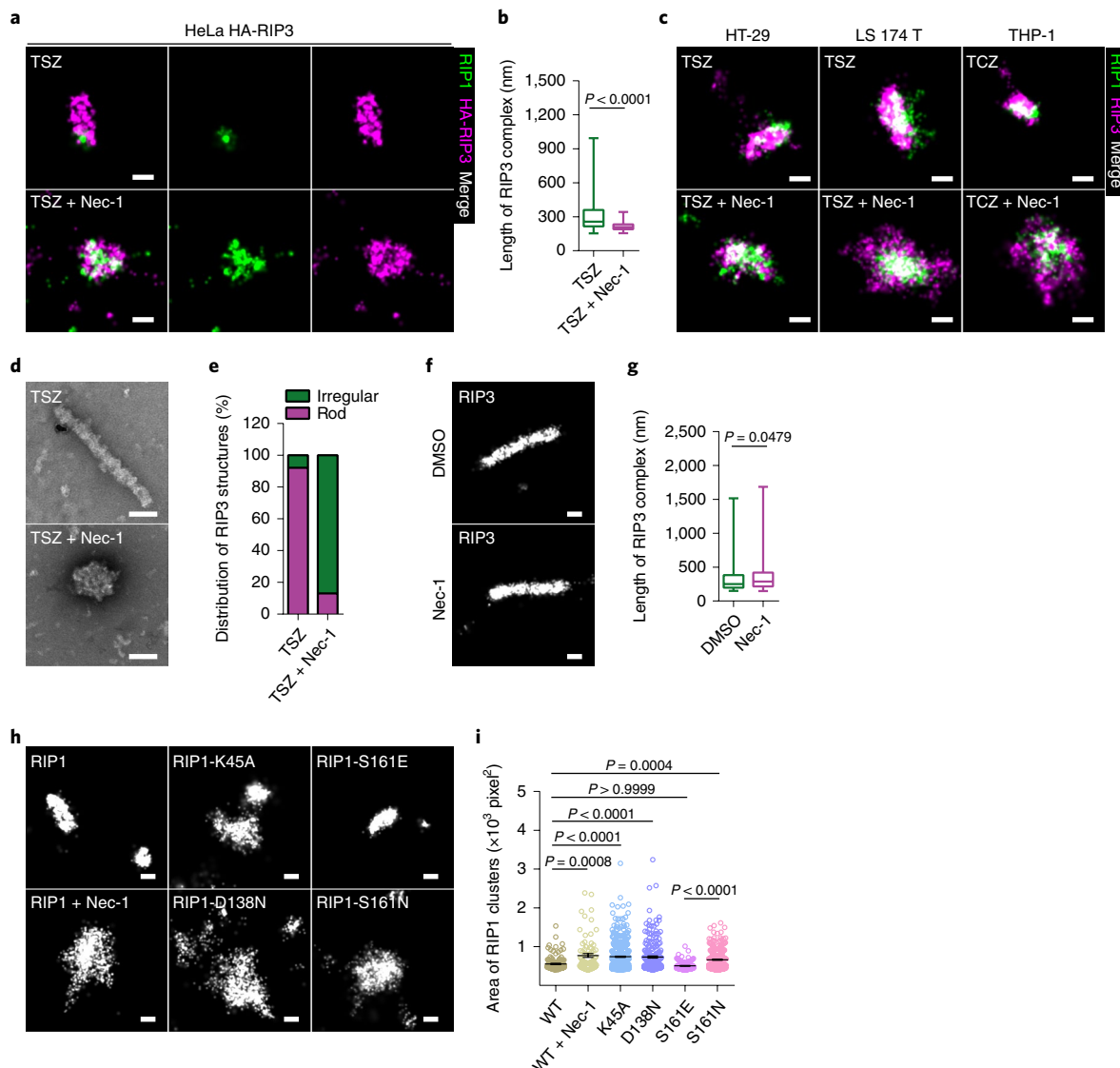


Fig. 5 | RIP1 kinase activity is required for RIP1 and RIP3 oligomerization in proper configuration that leads to the formation of functional rod-shaped complexes. **a,b**, Two-colour STORM images (**a**) and length distribution (**b**) of TSZ-induced RIP1-RIP3 complexes in the absence ($n=240$ structures) or presence ($n=235$ structures) of Nec-1. **c**, Two-colour STORM images of RIP1-RIP3 complexes in HT-29, LS 174 T or THP-1 cells treated as indicated. THP-1 cells were primed by 100 nM PMA. The experiment was performed three times with similar results. **d,e**, Negative-stain EM (**d**) and structure distribution (**e**) of RIP3 complexes isolated in Flag-RIP3-expressing HeLa cells treated with TSZ ($n=38$ structures) or TSZ plus Nec-1 ($n=23$ structures). **f,g**, STORM images (**f**) and length distribution (**g**) of overexpressed RIP3 complexes in *RIP1*-KO HeLa cells treated with DMSO ($n=264$ structures) or Nec-1 ($n=996$ structures). **h,i**, STORM images (**h**) and area distribution (**i**) of RIP1-WT or mutants overexpressed in *RIP1*-KO HeLa cells with or without Nec-1 treatment ($n=122$ structures for WT, $n=77$ structures for WT + Nec-1, $n=439$ structures for K45A, $n=217$ structures for D138N, $n=129$ structures for S161E and $n=283$ structures for S161N, shown as mean \pm s.e.m.). Data in **b,e,g** are pooled from four, two, two and three independent experiments, respectively, that yielded similar results. Box plots (**b,g**) show median and 25th to 75th percentiles, and whiskers indicate the minimum and maximum values. P values are determined by two-tailed, unpaired *t*-test (**b,g**), or by Kruskal-Wallis test with Dunn's multiple comparisons test (**i**). Scale bars, 100 nm. Statistical source data are provided in Source Data Fig. 5. Also see Extended Data Fig. 7.

necrosome rods about 47 nm in width and 33 nm in pitch length (Extended Data Fig. 10a, (II)); RIP1 and RIP3 homo-oligomers distribute heterogeneously in the rod-shaped necrosome with a mosaic pattern (Extended Data Fig. 10a, (III)). An updated summary for the regulation of necroptosis or apoptosis by necrosome is shown in Extended Data Fig. 10b. It is known that the interplay between RIP1 and RIP3 plays an essential role in the decision of apoptosis or necroptosis^{4,43–48}. The mosaic is likely to be the structural basis for the signalling divarication to necroptosis and apoptosis. RIP3 domains in the mosaic rods appear to be responsible for the signal to necrop-

tosis and the RIP1 domains might be responsible for signalling to apoptosis under the condition of RIP3 D161N mutation or GSK872 presence. Although ectopic overexpression of either RIP1 or RIP3 alone can form corresponding homo-oligomer to trigger apoptosis and necroptosis, respectively, a special configuration relying on RIP1 autophosphorylation is required for RIP1 to initiate functional RIP3 oligomer for necroptosis (Fig. 5) and a RIP3 D161N mutation- or GSK872-dependent conformation is required for RIP3 oligomer to initiate apoptosis via RIP1 (Fig. 7). Autophosphorylation of RIP3 is required for RIP3 to recruit and phosphorylate MLKL,

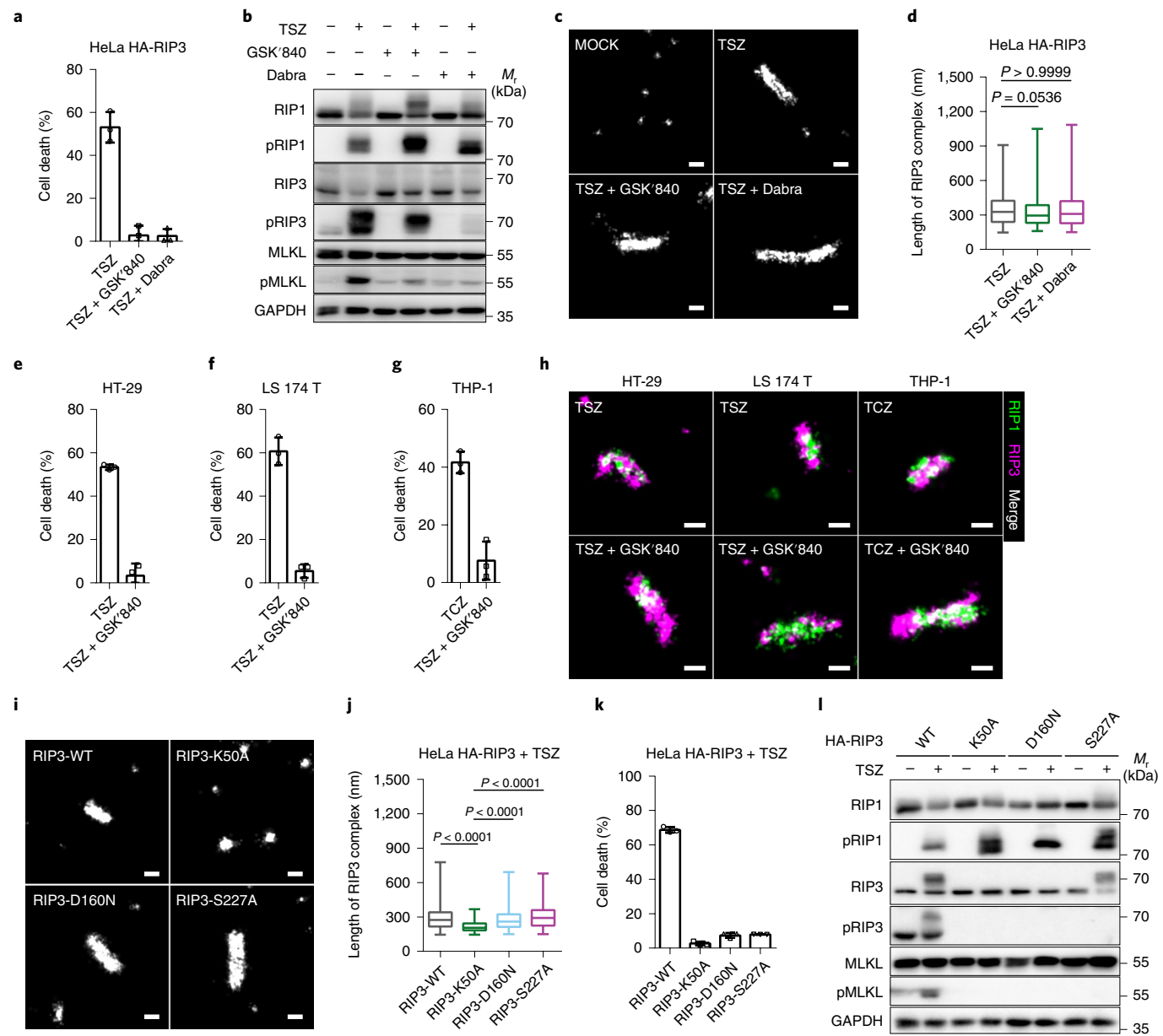


Fig. 6 | RIP3 autophosphorylation is dispensable for the formation of rod-shaped complex. **a-d**, HA-RIP3-expressing HeLa cells were treated as indicated (GSK'840, 5 μ M; Dabra, 5 μ M). Cell viability was measured, and data are represented as mean \pm s.d. of biological triplicates (**a**). Cell lysates were collected and subjected to western blot analysis for the indicated proteins (**b**). Single-colour STORM images (**c**) and length distribution (**d**; $n = 489$ structures for TSZ, $n = 288$ structures for TSZ + GSK'840 and $n = 620$ structures for TSZ + Dabra) of RIP3 structures in cells from **b**. **e-g**, Viability of HT-29 (**e**), LS 174 T (**f**) and THP-1 (**g**) cells treated as indicated. THP-1 cells were primed by 100 nM PMA. Data are represented as mean \pm s.d. of biological triplicates. **h**, Two-colour STORM images of RIP1-RIP3 complex in cells from **e-g**. **i-l**, HeLa cells expressing RIP3 WT or mutants were treated with DMSO or TSZ. Single-colour STORM images (**i**) and length distribution (**j**; $n = 439$ structures for WT, $n = 603$ structures for K50A, $n = 1,173$ structures for D160N and $n = 1,002$ structures for S227A) of RIP3 structures are shown. Cell viability was measured, and data are represented as mean \pm s.d. of biological triplicates (**k**). Cell lysates were collected and subjected to western blot analysis for the indicated proteins (**l**). Immunoblotting in **b** and **l** are representative of five and four independent experiments, respectively. Data in **d** and **j** are pooled from three independent experiments that yielded similar results. Box plots (**d**, **j**) show median and 25th to 75th percentiles, and whiskers indicate the minimum and maximum values. P values are determined by Kruskal-Wallis test with Dunn's multiple comparisons test (**d**, **j**). Scale bars, 100 nm. Unprocessed blots and statistical source data are provided in Source Data Fig. 6. Also see Extended Data Fig. 8.

and the defects in this event result in enlarged RIP1–RIP3 complex and necroptosis blockade¹⁹. Similarly, dephosphorylation of RIP3 by PPM1B inhibits necroptosis but does not promote apoptosis⁴⁰. Therefore, the reverse signalling to apoptosis in necrosome requires a special configuration of RIP3, and eliminating RIP3 phosphorylation is not sufficient. The structure of GSK'872-bound RIP3 should

give a clue of what this special configuration of RIP3 is. Although the functional structures of RIP1 and RIP3 in their oligomers have not been solved, mosaic rod shape is the hallmark of functional necrosome at nanometre scale.

It is reported that the RHIM fragments of RIP1 and RIP3 preferentially form hetero-complex²⁵. However, our super-resolution

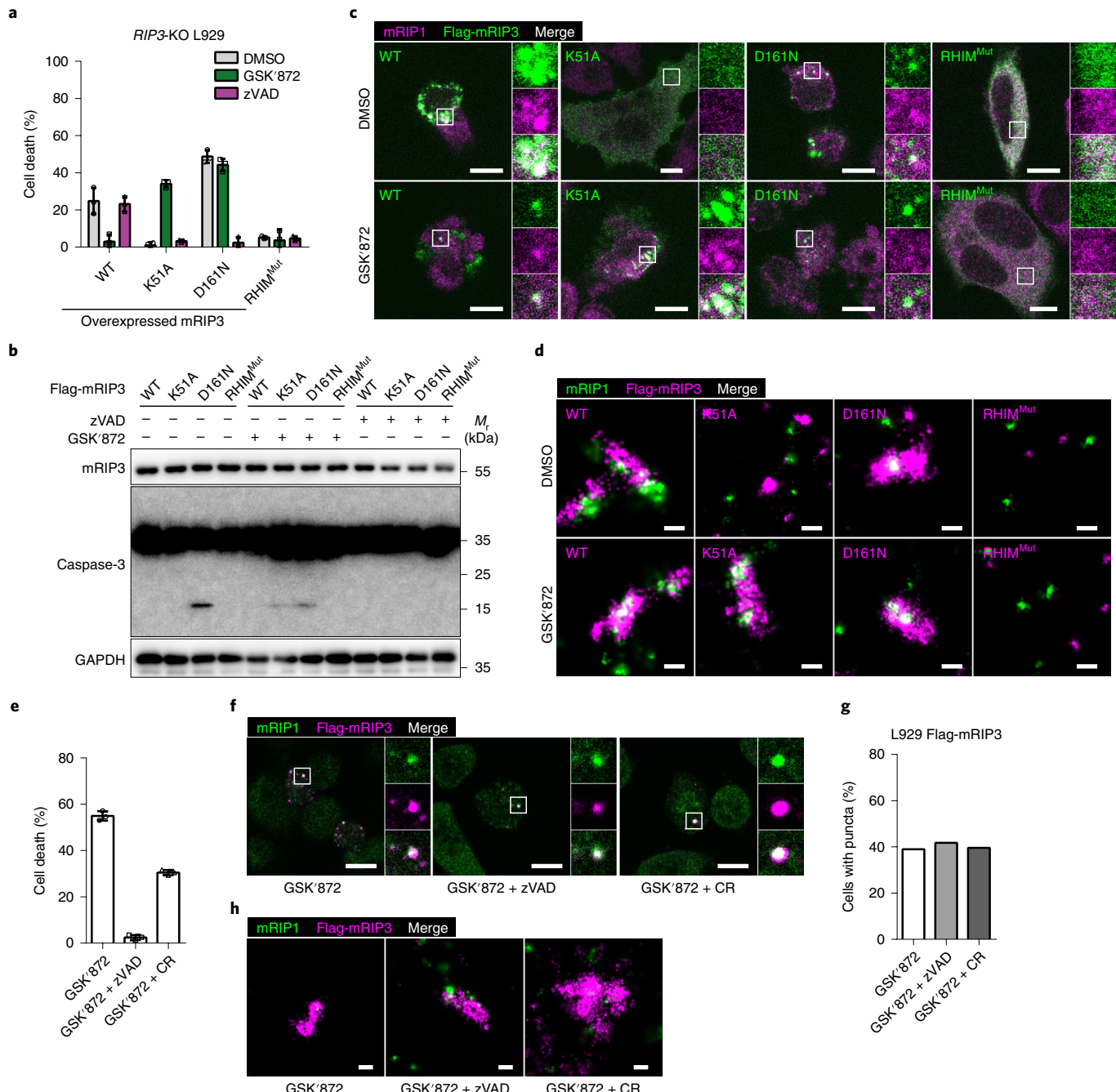


Fig. 7 | Apoptosis triggered by RIP3 kinase inhibition relies on the mosaic structure composed of RIP1 oligomer. **a-d**, Flag-mRIP3 WT or mutants (K51A, D161N or RHIM^{Mut}) were expressed in RIP3-deficient L929 cells and treated as indicated (DMSO, 5 μ M GSK'872 or 20 μ M zVAD). Cell viability was measured, and data are represented as means \pm s.d. of biological triplicates (**a**). Cell lysates were collected and subjected to western blot analysis for the indicated proteins (**b**). The experiment was performed three times with similar results. Confocal (**c**) and STORM (**d**) images of mRIP1 and mRIP3 in cells treated as in **a**. **e-h**, Flag-mRIP3-reconstituted RIP3-deficient L929 cells were treated by chemicals as indicated (5 μ M GSK'872, 100 μ M CR or 20 μ M zVAD). Cell viability was measured, and data are represented as means \pm s.d. of biological triplicates (**e**). Confocal (**f**) and STORM (**h**) images of mRIP1 and mRIP3 in cells treated as in **e**. Percentages of cells with RIP3 puncta in **f** were calculated (**g**). *n*=82–103 cells pooled by two independent experiments. Scale bars, 10 μ m (**c,f**) and 100 nm (**d,h**). Unprocessed blots and statistical source data are provided in Source Data Fig. 7. Also see Extended Data Fig. 9.

imaging showed that RIP1 and RIP3 homo-clusters are the predominant portions of necrosomes in necroptotic cells, suggesting the formation of RIP1/RIP3 homo-oligomers is energetically more favourable than that of RIP1–RIP3 hetero-oligomers. Supportively, a recent solid-state NMR study revealed that the amyloid fibril structure of RIP3 RHIM-containing domain differs from previ-

ously published RIP1/RIP3 hetero-amyloid complex structure⁴⁹. Moreover, mechanism(s) other than RHIM domain interaction contribute to the formation of RIP1–RIP3 necrosomes. For instance, the death domain of RIP1 can also mediate RIP1–RIP1 interaction^{34,50}. Herein we demonstrate that RIP1 autophosphorylation is not only required for RIP1 oligomerization in proper order

but also determines RIP1-initiated RIP3 homo-oligomerization in a correct way that leads to the formation of rod-shaped necrosome (Fig. 5). RIP1 can be phosphorylated by several kinases such as TAK1 and MK2 that promote and inhibit RIP1-mediated cell death, respectively^{51–53}. RIP1 also can be ubiquitylated at many sites with diverse functions⁵⁴. Modifications of RIP1 appear to affect the structure of RIP1, and some of them may influence the organization of RIP1 oligomers and therefore have impacts on the RIP3 oligomers in necrosome mosaics.

Upon phosphorylation by RIP3, MLKL is believed to form oligomers, which then move to the plasma membrane and trigger cell death^{10–13}. However, overexpressed RIP3-RHIM^{Mut} with a defect in oligomerization still phosphorylated MLKL to a level comparable to that by oligomerized RIP3 (Fig. 3). Thus, phosphorylation and oligomerization of MLKL are not automatically coupled. Our results demonstrate that oligomerization of RIP3, or more precisely RIP3 oligomer with sizes of tetramer or above, is required for MLKL oligomerization and cell death (Fig. 4). As the ratio of RIP3 to MLKL in the crystal structure is 1:1²⁶ and MLKL in necroptotic cells indeed was detected as tetramer by non-reducing SDS-PAGE¹⁰, the threshold size of RIP3 oligomer revealed here uncovers the missing step of RIP3–MLKL interaction required for functional MLKL oligomer.

Finally, our work emphasizes the importance of applying super-resolution imaging to understand the nanoscale necrosome-like signalosomes, as it provides much previously uncovered structural information. The clear link between intact ordered structure of mosaic necrosomes and cell death induction also highlights a possible therapeutic intervention for necroptosis/apoptosis-related human diseases by disrupting the architecture of necrosomes.

Online content

Methods, additional references, Nature Research reporting summaries, source data, extended data, supplementary information, acknowledgements, peer review information; details of author contributions and competing interests; and statements of data and code availability are available at <https://doi.org/10.1038/s41556-022-00854-7>.

Received: 8 April 2021; Accepted: 26 January 2022;

Published online: 07 March 2022

References

1. Weinlich, R., Oberst, A., Beere, H. M. & Green, D. R. Necroptosis in development, inflammation and disease. *Nat. Rev. Mol. Cell Biol* **18**, 127–136 (2017).
2. Wang, L., Du, F. H. & Wang, X. D. TNF- α induces two distinct caspase-8 activation pathways. *Cell* **133**, 693–703 (2008).
3. Wilson, N. S., Dixit, V. & Ashkenazi, A. Death receptor signal transducers: nodes of coordination in immune signaling networks. *Nat. Immunol.* **10**, 348–355 (2009).
4. Zhang, D. W. et al. RIP3, an energy metabolism regulator that switches TNF-induced cell death from apoptosis to necrosis. *Science* **325**, 332–336 (2009).
5. He, S. D. et al. Receptor interacting protein kinase-3 determines cellular necrotic response to TNF- α . *Cell* **137**, 1100–1111 (2009).
6. Cho, Y. et al. Phosphorylation-driven assembly of the RIP1–RIP3 complex regulates programmed necrosis and virus-induced inflammation. *Cell* **137**, 1112–1123 (2009).
7. Yang, Z. H. et al. A non-canonical PDK1-RSK signal diminishes pro-caspase-8-mediated necroptosis blockade. *Mol. Cell* **80**, 296 (2020).
8. Sun, L. et al. Mixed lineage kinase domain-like protein mediates necrosis signaling downstream of RIP3 kinase. *Cell* **148**, 213–227 (2012).
9. Zhao, J. et al. Mixed lineage kinase domain-like is a key receptor interacting protein 3 downstream component of TNF-induced necrosis. *Proc. Natl Acad. Sci. USA* **109**, 5322–5327 (2012).
10. Chen, X. et al. Translocation of mixed lineage kinase domain-like protein to plasma membrane leads to necrotic cell death. *Cell Res.* **24**, 105 (2014).
11. Cai, Z. Y. et al. Plasma membrane translocation of trimerized MLKL protein is required for TNF-induced necroptosis. *Nat. Cell Biol.* **16**, 200 (2014).
12. Wang, H. et al. Mixed lineage kinase domain-like protein MLKL causes necrotic membrane disruption upon phosphorylation by RIP3. *Mol. Cell* **54**, 133–146 (2014).
13. Dondelinger, Y. et al. MLKL compromises plasma membrane integrity by binding to phosphatidylinositol phosphates. *Cell Rep.* **7**, 971–981 (2014).
14. Degterev, A. et al. Chemical inhibitor of nonapoptotic cell death with therapeutic potential for ischemic brain injury. *Nat. Chem. Biol.* **1**, 112–119 (2005).
15. Degterev, A. et al. Identification of RIP1 kinase as a specific cellular target of necrostatins. *Nat. Chem. Biol.* **4**, 313–321 (2008).
16. Hitomi, J. I. et al. Identification of a molecular signaling network that regulates a cellular necrotic cell death pathway. *Cell* **135**, 1311–1323 (2008).
17. Holler, N. et al. Fas triggers an alternative, caspase-8-independent cell death pathway using the kinase RIP as effector molecule. *Nat. Immunol.* **1**, 489–495 (2000).
18. Sun, X. Q., Yin, J. P., Starovasnik, M. A., Fairbrother, W. J. & Dixit, V. M. Identification of a novel homotypic interaction motif required for the phosphorylation of receptor-interacting protein (RIP) by RIP3. *J. Biol. Chem.* **277**, 9505–9511 (2002).
19. Chen, W. Z. et al. Diverse sequence determinants control human and mouse receptor interacting protein 3 (RIP3) and mixed lineage kinase domain-like (MLKL) interaction in necroptotic signaling. *J. Biol. Chem.* **288**, 16247–16261 (2013).
20. Hildebrand, J. M. et al. Activation of the pseudokinase MLKL unleashes the four-helix bundle domain to induce membrane localization and necroptotic cell death. *Proc. Natl Acad. Sci. USA* **111**, 15072–15077 (2014).
21. Petrie, E. J. et al. Conformational switching of the pseudokinase domain promotes human MLKL tetramerization and cell death by necroptosis. *Nat. Commun.* **9**, 2422 (2018).
22. Mandal, P. et al. RIP3 induces apoptosis independent of pronecrotic kinase activity. *Mol. Cell* **56**, 481–495 (2014).
23. Newton, K. et al. Activity of protein kinase RIPK3 determines whether cells die by necroptosis or apoptosis. *Science* **343**, 1357–1360 (2014).
24. Li, J. et al. The RIP1/RIP3 necrosome forms a functional amyloid signaling complex required for programmed necrosis. *Cell* **150**, 339–350 (2012).
25. Monpéan, M. et al. The structure of the necrosome RIPK1–RIPK3 core, a human hetero-amyloid signaling complex. *Cell* **173**, 1244–1253.e1210 (2018).
26. Xie, T. et al. Structural insights into RIP3-mediated necroptotic signaling. *Cell Rep.* **5**, 70–78 (2013).
27. Murphy, J. M. et al. The pseudokinase MLKL mediates necroptosis via a molecular switch mechanism. *Immunity* **39**, 443–453 (2013).
28. Rust, M. J., Bates, M. & Zhuang, X. W. Sub-diffraction-limit imaging by stochastic optical reconstruction microscopy (STORM). *Nat. Methods* **3**, 793–795 (2006).
29. Huang, B., Wang, W. Q., Bates, M. & Zhuang, X. W. Three-dimensional super-resolution imaging by stochastic optical reconstruction microscopy. *Science* **319**, 810–813 (2008).
30. Sigal, Y. M., Zhou, R. B. & Zhuang, X. W. Visualizing and discovering cellular structures with super-resolution microscopy. *Science* **361**, 880–887 (2018).
31. Malkusch, S. & Heilemann, M. Extracting quantitative information from single-molecule super-resolution imaging data with LAMA—LocAlization Microscopy Analyzer. *Sci. Rep.* **6**, 34486 (2016).
32. Berg, S. et al. ilastik: interactive machine learning for (bio) image analysis. *Nat. Methods* **16**, 1226–1232 (2019).
33. Bates, M., Huang, B., Dempsey, G. T. & Zhuang, X. W. Multicolor super-resolution imaging with photo-switchable fluorescent probes. *Science* **317**, 1749–1753 (2007).
34. Wu, X. N. et al. Distinct roles of RIP1–RIP3 hetero- and RIP3–RIP3 homo-interaction in mediating necroptosis. *Cell Death Differ.* **21**, 1709–1720 (2014).
35. Muthuswamy, S. K., Gilman, M. & Brugge, J. S. Controlled dimerization of ErbB receptors provides evidence for differential signaling by homo- and heterodimers. *Mol. Cell. Biol.* **19**, 6845–6857 (1999).
36. Clackson, T. et al. Redesigning an FKBP-ligand interface to generate chemical dimerizers with novel specificity. *Proc. Natl Acad. Sci. USA* **95**, 10437–10442 (1998).
37. Inobe, T. & Nukina, N. Rapamycin-induced oligomer formation system of FRB-FKBP fusion proteins. *J. Biosci. Bioeng.* **122**, 40–46 (2016).
38. Zhang, Y. et al. RIP1 autoprophosphorylation is promoted by mitochondrial ROS and is essential for RIP3 recruitment into necrosome. *Nat. Commun.* **8**, 14329 (2017).
39. Li, J. X. et al. The B-Raf^{V600E} inhibitor dabrafenib selectively inhibits RIP3 and alleviates acetaminophen-induced liver injury. *Cell Death Dis.* **5**, e1278 (2014).
40. Chen, W. Z. et al. Ppm1b negatively regulates necroptosis through dephosphorylating Rip3. *Nat. Cell Biol.* **17**, 434 (2015).
41. Harris, P. A. et al. Discovery of small molecule RIP1 kinase inhibitors for the treatment of pathologies associated with necroptosis. *ACS Med. Chem. Lett.* **4**, 1238–1243 (2013).
42. Ding, J. J. et al. Structural and functional insights into host death domains inactivation by the bacterial arginine GlcNAcyltransferase effector. *Mol. Cell* **74**, 922 (2019).

43. Dannappel, M. et al. RIPK1 maintains epithelial homeostasis by inhibiting apoptosis and necroptosis. *Nature* **513**, 90 (2014).
44. Dillon, C. P. et al. RIPK1 blocks early postnatal lethality mediated by caspase-8 and RIPK3. *Cell* **157**, 1189–1202 (2014).
45. Kaiser, W. J. et al. RIP1 suppresses innate immune necrotic as well as apoptotic cell death during mammalian parturition. *Proc. Natl Acad. Sci. USA* **111**, 7753–7758 (2014).
46. Orozco, S. et al. RIPK1 both positively and negatively regulates RIPK3 oligomerization and necroptosis. *Cell Death Differ.* **21**, 1511–1521 (2014).
47. Rickard, J. A. et al. RIPK1 regulates RIPK3-MLKL-driven systemic inflammation and emergency hematopoiesis. *Cell* **157**, 1175–1188 (2014).
48. Roderick, J. E. et al. Hematopoietic RIPK1 deficiency results in bone marrow failure caused by apoptosis and RIPK3-mediated necroptosis. *Proc. Natl Acad. Sci. USA* **111**, 14436–14441 (2014).
49. Wu, X. L. et al. The amyloid structure of mouse RIPK3 (receptor interacting protein kinase 3) in cell necroptosis. *Nat. Commun.* **12**, 1627 (2021).
50. Meng, H. Y. et al. Death-domain dimerization-mediated activation of RIPK1 controls necroptosis and RIPK1-dependent apoptosis. *Proc. Natl Acad. Sci. USA* **115**, E2001–E2009 (2018).
51. Jaco, I. et al. MK2 phosphorylates RIPK1 to prevent TNF-induced cell death. *Mol. Cell* **66**, 698 (2017).
52. Dondelinger, Y. et al. MK2 phosphorylation of RIPK1 regulates TNF-mediated cell death. *Nat. Cell Biol.* **19**, 1237–1247 (2017).
53. Geng, J. F. et al. Regulation of RIPK1 activation by TAK1-mediated phosphorylation dictates apoptosis and necroptosis. *Nat. Commun.* **8**, 359 (2017).
54. Meng, Y. X., Sandow, J. J., Czabotar, P. E. & Murphy, J. M. The regulation of necroptosis by post-translational modifications. *Cell Death Differ.* **28**, 861–883 (2021).

Publisher's note Springer Nature remains neutral with regard to jurisdictional claims in published maps and institutional affiliations.

© The Author(s), under exclusive licence to Springer Nature Limited 2022

Methods

Cell lines and cell culture. HeLa, HEK293T, HT-29, THP-1 and mouse fibrosarcoma L929 cells were obtained from the American Type Culture Collection. LS 17/4T cells were a kind gift from Dr Sudan He (Suzhou Institute of Systems Medicine, China). *RIP3*-KO L929 and HT-29 cells were established previously^{19,55}. *RIP1*-KO or *MLKL*-KO HeLa, and *MLKL*-KO HT-29, cell lines were generated by using CRISPR/Cas9 method. The disruption of target gene was determined by the sequencing of gene loci and by the immunoblotting of cell lysates with antibodies. All cell lines were maintained at 37 °C and 5% CO₂ in DMEM (Invitrogen) supplemented with 10% fetal bovine serum (Gibco), 2 mM L-glutamine, 100 IU penicillin and 100 mg ml⁻¹ streptomycin. Cells were routinely tested to be free of mycoplasma contamination.

Plasmids, reagents and antibodies. Full-length and mutated RIP1, RIP3, MLKL and PPM1B with Flag or HA tag were cloned into the lentiviral vector pBOB (Addgene, 12337). The FV/FKBP/FRB-fused RIP3 WT or RHIM mutant was amplified by standard PCR from our complementary DNA library. All plasmids were verified by DNA sequencing. The details of the sequences are available upon request. Recombinant human and mouse TNF- α (PHC3011 and PMC3015) were from Thermo Fisher Scientific and used at 10 ng ml⁻¹. The following compounds were used: Smac mimetic SM-164 (APEXBio, A8815, 0.1 μ M), pan-caspase inhibitor Z-VAD-FMK (Calbiochem, 627610, 20 μ M), necrostatin-1 (EMD Chemicals, 480065, 5 μ M), GSK'840 (AOBIOUS, ABO917, 5 μ M), GSK'872 (MCE, HY-101872, 5 μ M), dabrafenib (Selleck, S2807, 5 μ M), cycloheximide (Sigma, C7698, 10 μ g ml⁻¹), doxycycline (Sigma, D9891, 1 μ g ml⁻¹), rapamycin (Selleck, S1039, 1 μ M), AP20187 (TaKaRa, 635069, 1 μ M), phorbol myristate acetate (PMA) (Sigma, P8139, 100 nM), CR (Sigma, 75768, 100 μ M), propidium iodide (Sigma, P4170, 2 μ g ml⁻¹) and Hoechst 33342 (Thermo Fisher Scientific, H1399, 1 μ g ml⁻¹). The following antibodies were used throughout this report: anti-RIP1 (Cell Signaling, 3493, 1:150 for immunofluorescence (IF), 1:1,000 for western blotting (WB)), anti-phospho Ser166 RIP1 (Cell Signaling, 65746, 1:1,000 for WB), anti-RIP3 (Santa Cruz, sc-374639, 1:150 for IF; Cell Signaling, 13526, 1:1,000 for WB), anti-phospho Ser227 RIP3 (Abcam, ab209384, 1:500 for IF; 1:1,000 for WB), anti-MLKL (Abcam, ab184718, 1:1,000 for WB), anti-phospho Ser358 MLKL (Abcam, ab187091, 1:200 for IF; 1:1,000 for WB), anti-Caspase-3 (Cell Signaling, 9662, 1:1,000 for WB), anti-PPM1B (Abcam, ab70804, 1:1,000 for WB), anti-HA (Santa Cruz, sc-7392, 1:200 for IF, 1:1,000 for WB; Cell Signaling, 3724, 1:200 for IF, 1:1,000 for WB), anti-Flag (Cell Signaling, 8146, 1:200 for IF, 1:1,000 for WB; Biologend, 637301, 1:200 for IF), anti-GAPDH (ABclonal, AC002, 1:5,000 for WB), goat anti-rabbit, anti-mouse and anti-rat secondary antibodies conjugated to Alexa Fluor 488, 568 or 647 (Thermo Fisher Scientific, A11034, A11004 or A21247, 1:1,000 for IF) and goat anti-rabbit and anti-mouse secondary antibodies conjugated to CF 568 or CF 647 (Biotium, 20800, 20801, 20808 or 20809, 1:500 for IF).

Transfection and lentiviral infection. Transfection of cells was performed using Turbofect reagent according to the manufacturer's instructions (Thermo Fisher Scientific, R0531). For lentivirus production, HEK293T cells were transfected with lentiviral vectors and virus-packing plasmids by the calcium phosphate precipitation method. The virus-containing medium was collected 36–48 h later and added to L929, HeLa or other cells as indicated with 10 μ g ml⁻¹ of polybrene. The infectious medium was changed with fresh medium 12 h later, and cells were kept in culture until analysis.

Cell viability assay. Cell viability was determined by FACS or CellTiter-Glo Luminescent Cell Viability Assay Kit (Promega, G7571). FACS was performed as previously described⁴. In brief, cells were trypsinized, re-suspended in PBS containing 5 μ g ml⁻¹ propidium iodide (PI) and quantified on a FACS Calibur flow cytometer with CellQuest Pro software. PI-negative cells with normal size were considered as living cells. The luminescent cell viability assays were performed according to the manufacturer's instructions. In brief, 1.0 \times 10⁵ cells were seeded in 96-well plates with white wall. After treatment, an equal volume of CellTiter-Glo reagent was added to the cell culture medium, which had been equilibrated to room temperature for 30 min. Cells were shaken for 5 min and incubated at room temperature for 15 min. Luminescent recording was performed with POLAR star Omega (BMG Labtech).

Immunoprecipitation and immunoblotting. Cell pellets were obtained in ice-cold PBS and re-suspended in lysis buffer (20 mM Tris-HCl pH 7.5, 150 mM NaCl, 1 mM Na₂EDTA, 1 mM EGTA, 1% Triton X-100, 2.5 mM sodium pyrophosphate, 1 mM β -glycerophosphate and 1 mM Na₃VO₄) plus protease inhibitor cocktail (MCE, HY-K0010). The re-suspended cell pellets were sonicated and centrifuged at 20,000g for 30 min at 4 °C. The supernatant was immunoprecipitated with Flag-M2 affinity resin (Sigma, A2220) at 4 °C for 3 h or overnight. After the immunoprecipitation, the beads were washed four times in lysis buffer and the immunoprecipitates were subsequently eluted with Flag peptide or SDS sample buffer (50 mM Tris pH 6.8, 2% SDS, 5% β -mercaptoethanol, 0.02% bromophenol blue and 10% glycerol). MLKL tetramer is separated by non-reducing PAGE as previously reported¹⁰. In brief, cells were directly treated with SDS sample buffer

without β -mercaptoethanol, and the sample was heated at 100 °C for 5 min and resolved by 4–12% gradient NuPAGE (Invitrogen, NP0336BOX). To analyse RIP3 oligomeric status, cells were permeabilized in buffer (20 mM HEPES pH 7.5, 100 mM KCl, 2.5 mM MgCl₂ and 100 mM sucrose) containing 1% digitonin and protease inhibitors. Samples were collected by centrifugation (25 min at 11,000g) and resolved on a 3–12% NativePAGE gel (Invitrogen, BN1003BOX). After electrophoresis, protein samples were transferred onto PVDF membranes. Membranes were blocked with 3% BSA for 1 h and incubated with primary antibodies as indicated for 2 h at room temperature, followed by incubation with horseradish peroxidase-conjugated secondary antibodies. Proteins were visualized using the blot and gel imager (AI680, GE Healthcare). GAPDH was used as a loading control.

Negative-stain EM and AFM. To visualize necosome at nanoscale, RIP3 complex was induced in Flag-RIP3-expressing HeLa cells challenged by TSZ, or generated by overexpression of Flag-RIP3 in HeLa cells. As described above, RIP3 complex was collected using Flag-M2 affinity resin. For EM, the protein solution was blotted on EM grids, negatively stained with 2% uranium hydrogen acetate and imaged with HT 7800 electron microscope (Hitachi, Japan) operated at 80 kV. For AFM, the protein solution was deposited onto freshly cleaved mica surface and air dried. AFM characterizations were performed on a Bruker Nanowizard4-XP Scanning Probe Microscope with a Vortis2 SPM Controller (Bruker, BioAFM). Al-coated silicon AFM tips (SNL-10, Bruker, BioAFM) were used to probe the surface profiles of the rod-shaped necosome. Tapping-mode AFM imaging was used according to well-established procedures. All the images were post-treated with JPKSPM Data Processing Software.

Confocal microscopy. For immunostaining, cells were grown on #1.5 coverslips (NEST, 801008) coated with poly-L-lysine (Sigma, P1399). Cells were fixed with freshly prepared 3.7% formaldehyde for 15 min at room temperature and then permeabilized with 0.2% Triton X-100 in PBS. After being blocked with 3% BSA for 30 min, the samples were stained with primary antibodies at 4 °C overnight, washed three times with PBS and incubated with secondary antibodies for 1 h at room temperature. The slides were mounted with antifade reagent (Invitrogen, P36934). For imaging with multiple channels, extensive controls were performed to make sure there was no non-specific staining or crosstalk between channels. These controls include (1) using cells that lack one of the proteins of interest and/or (2) performing staining without one of the primary or secondary antibodies. All images were captured and processed using identical settings in the LSM 780 laser scanning confocal microscope (ZEN 2012, Zeiss) with a 63 \times /1.40 numerical aperture (NA) oil objective. Duplicate cultures were examined, and similar results were obtained in at least two independent experiments.

STORM imaging. STORM imaging was performed on an N-STORM microscope (Ti-E, Nikon Instruments). Briefly, the N-STORM system uses an Agilent MLC-400B laser launch with a red diode laser (647 nm, 300 mW; MPBC), a green solid-state laser (561 nm, 150 mW; Coherent), a blue solid-state laser (488 nm, 200 mW; Coherent), a violet diode laser (405 nm, 100 mW; Coherent) and a 100 \times NA 1.49 oil immersion objective. The emission fluorescence was separated using appropriate filters (FF02-520/28-25, FF01-586/20-25 \times 3.5 and FF01-692/40-25; Semrock) and detected by a back-illuminated EMCCD camera (iXon DU897, Andor). Cells were pre-cultured on an eight-well chambered cover glass (Thermo Fisher Scientific, 155409). Sample preparation for STORM imaging is similar to the procedure for confocal microscopy. But in the case of pRIP3 staining, we used methanol fixation (-20 °C for 10 min) instead to reduce the background signal. After being labelled with appropriate fluorescence-conjugated antibodies, samples were immersed in an imaging buffer that contained 50 mM Tris (pH 8.0), 10 mM NaCl, 0.5 mg ml⁻¹ glucose oxidase (Sigma, G2133), 40 μ g ml⁻¹ catalase (Sigma, C40), 10% (wt/vol) glucose and 143 mM β -mercaptoethanol. For single-colour STORM imaging of CF 647, cells were exposed to a 647 nm laser at a power density of 2 kW cm⁻². For two-colour STORM imaging, the CF 647 channel was first recorded, and then the CF 568 channel was acquired with a laser power density of 1–3 kW cm⁻². A 405 nm laser was ramped during the image capture to maintain proper blinking frequency. Typically, 10,000–20,000 frames for each channel were collected at a rate of 70 fps, and images were reconstructed using the N-STORM module in NIS-Elements AR software. Chromatic alignment of STORM images was ensured by calibrating the system using 100 nm multi-fluorescent beads and following the chromatic calibration procedure in the Nikon software (NIS-Elements AR with an N-STORM module). Sample drift between frames was corrected by tracking multi-fluorescent beads (Thermo Fisher Scientific, T7279) or using image correlation. Identical settings were used for every image. Each localization is depicted in the STORM image as a Gaussian peak, the width of which is determined by the number of photons detected.

STORM image analysis. For the cluster analysis, we used a recently developed machine-learning-based segmentation toolkit, ilastik³². Briefly, high-quality STORM images were applied to ilastik segmentation workflow. Based on the feature descriptors, the classification of the effective signals was made and distinguished from noise. Each effective cluster was segmented and identified as

a strictly separated object. For single-colour STORM images, the training strategy for machine-learning-based segmentation is distinguishing the whole structure from background noise, while in some two-colour STORM experiments our goal is to isolate the subunits of RIP1/RIP3/MLKL within targeted structures. We cannot completely eliminate merging events of clusters, but these unwanted effects were reduced substantially by this procedure. Analysis parameters were determined by evaluating the segmentation outcomes. Once determined, these parameters were held constant across all images and conditions being compared. The output binary images were further processed in Fiji/ImageJ by extracting the Feret parameters and area of effective clusters. To identify the subunits of RIP1/RIP3/MLKL cluster in the same complex, the distance between the centroid of each subunit and their area was used to calculate the possibility of co-clustering in single-colour images or overlap between two-colour images. The effective cluster information, including the area and Feret parameters, was extracted, and statistics on the interested structures were calculated.

Molecular modelling. The published structures of RIP1–RIP3 hetero-amyloid core (Protein Data Bank (PDB) [5V7Z](#)), RIP1 kinase domain (PDB [4NEU](#)), RIP1 death domain (PDB [6AC5](#)) and RIP3 kinase domain (PDB [4M66](#)) were used in structural modelling and generating figures. The hetero-amyloid structure of RIP1–RIP3 in the published paper²⁵ showed a slight twist with an angle of $5.4^\circ \pm 0.5^\circ$ for RIP3 layers and $5.3^\circ \pm 0.3^\circ$ for RIP1 layers, respectively. To generate the proposed RIP1–RIP3 model, the initial helical rise and twist angle of structure containing two layers of RIP3 and two layers of RIP1 (derived from PDB 5v7z) were set to 19.5 \AA and 10.6° , respectively. Energy minimization was subsequently applied with TrRosetta⁵⁶ to optimize steric hindrance and clash in the model. Pymol (The PyMOL Molecular Graphics System, Version 2.4 Schrödinger) was used to generate all the figures.

Statistics and reproducibility. Statistical analysis was performed with Prism software. Error bars represent mean \pm s.e.m. or mean \pm s.d., as indicated. For the comparison of two datasets, data were analysed by two-tailed unpaired Student's *t*-test. To compare more than two datasets, we used Kruskal–Wallis test with two-sided Dunn's multiple comparison test. Sample size and the number of biological replicates for each experiment are indicated in the figure legends. STORM imaging, EM and western blot experiments were performed three times unless specified in the legends.

Reporting Summary. Further information on research design is available in the Nature Research Reporting Summary linked to this paper.

Data availability

The published structures of RIP1–RIP3 hetero-amyloid core (PDB [5V7Z](#)), RIP1 kinase domain (PDB [4NEU](#)), RIP1 death domain (PDB [6AC5](#)) and RIP3 kinase domain (PDB [4M66](#)) are accessible in the PDB (<https://www.rcsb.org/>) with respective IDs. Numerical source data giving rise to graphical representations and unprocessed images of blots are shown in source data figures. Detailed experimental procedures and additional data supporting the findings of this study

are available from the corresponding author on reasonable request. Source data are provided with this paper.

Code availability

All Python scripts and Fiji macros for STORM image analysis are available in the online repository GitHub (<https://github.com/xchenxmu/STORMing-the-necosome>).

References

55. Huang, Z. et al. RIP1/RIP3 binding to HSV-1 ICP6 initiates necroptosis to restrict virus propagation in mice. *Cell Host Microbe* **17**, 229–242 (2015).
56. Yang, J. Y. et al. Improved protein structure prediction using predicted interresidue orientations. *Proc. Natl. Acad. Sci. USA* **117**, 1496–1503 (2020).

Acknowledgements

This work was supported by the National Natural Science Foundation of China (81788101, 31420103910 and 81630042 to J.H.; 31871386, 31501115 and 32070736 to X.C.; 12090052 and 11874310 to J.S.), National Key R&D Program of China (2020YFA0803500 to J.H.), the 111 Project (B12001 to J.H.), the CAMS Innovation Fund for Medical Science (2019-I2M-5-062 to J.H.) and the China Postdoctoral Science Foundation (2016T90598 to X.C.). We thank L. Yao and C. Wu for help with electron microscopy; Q. Liu and Y. Fan (Bruker) for their assistance with confocal microscopy and AFM, respectively. We also acknowledge C. Zhou and L. Wang from Nikon for support and helpful discussions on super-resolution imaging.

Author contributions

X.C. carried out the majority of experimental work with the help of W.W., Y.C. and H.C. R.Z. performed molecular modelling. J.Z., X.L., Y.Y. and J.S. carried out the analysis of super-resolution images. X.C. and J.H. designed experiments, interpreted data and wrote the manuscript. J.H. conceived and supervised the study.

Competing interests

The authors declare no competing interests.

Additional information

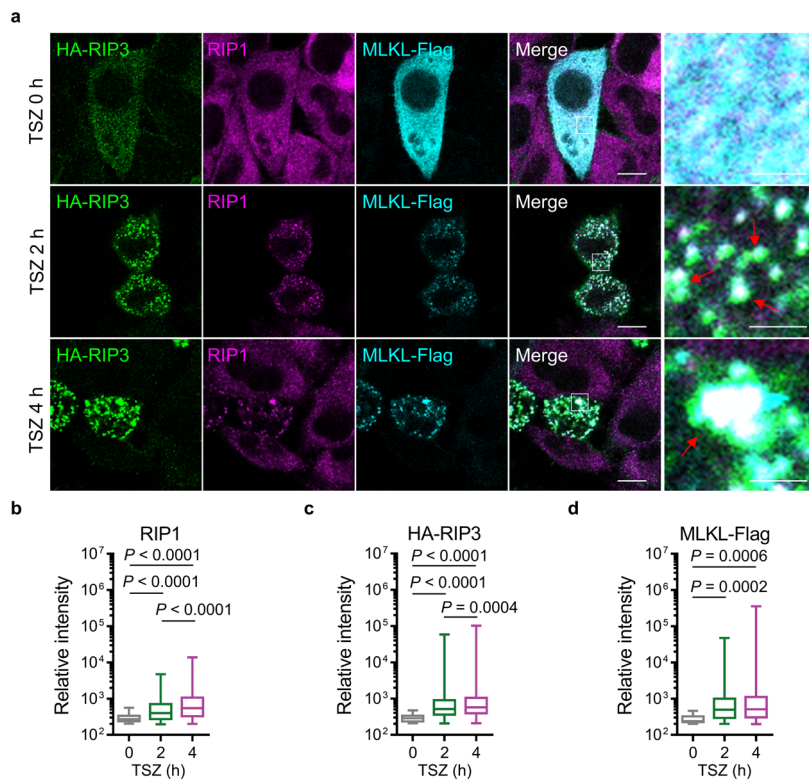
Extended data is available for this paper at <https://doi.org/10.1038/s41556-022-00854-7>.

Supplementary information The online version contains supplementary material available at <https://doi.org/10.1038/s41556-022-00854-7>.

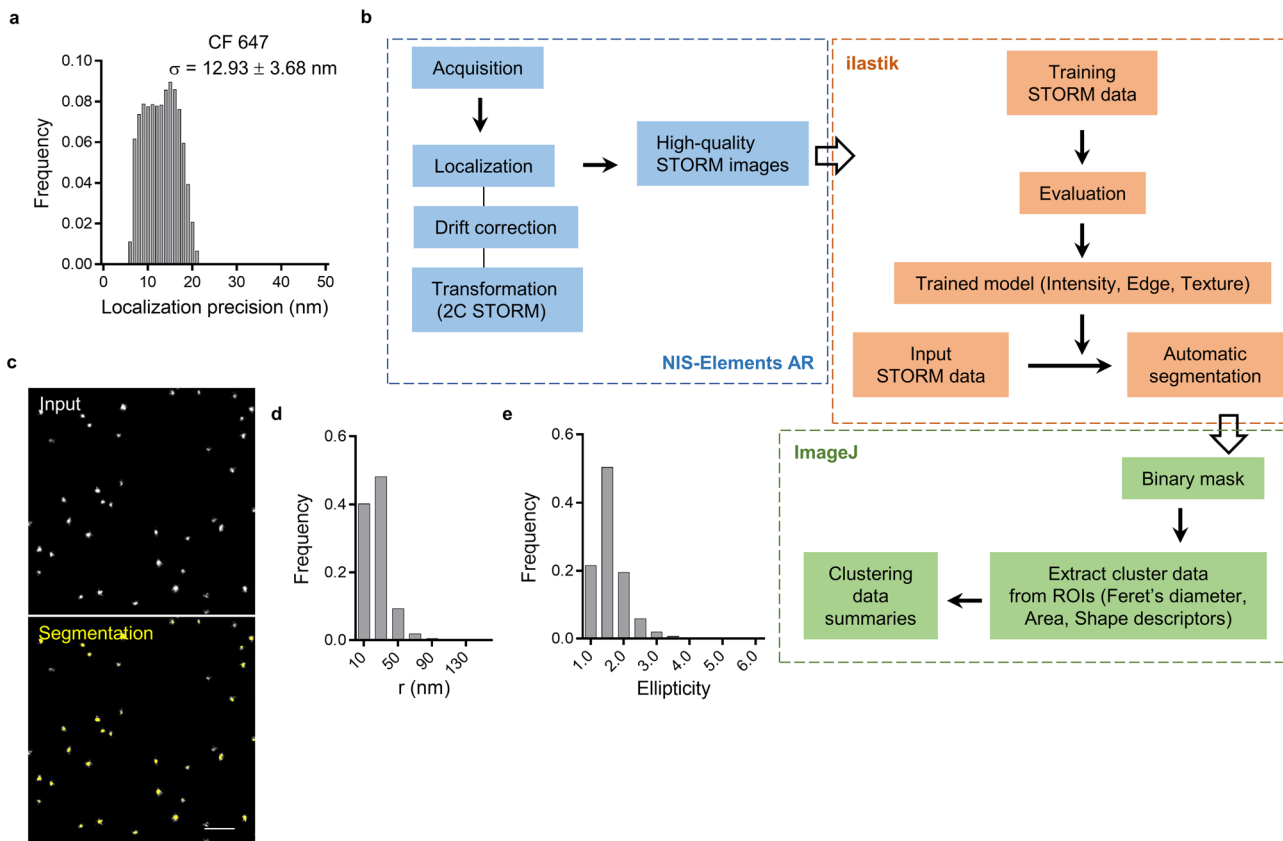
Correspondence and requests for materials should be addressed to Xin Chen or Jiahui Han.

Peer review information *Nature Cell Biology* thanks Sang-Hee Shim and the other, anonymous, reviewer(s) for their contribution to the peer review of this work. Peer reviewer reports are available.

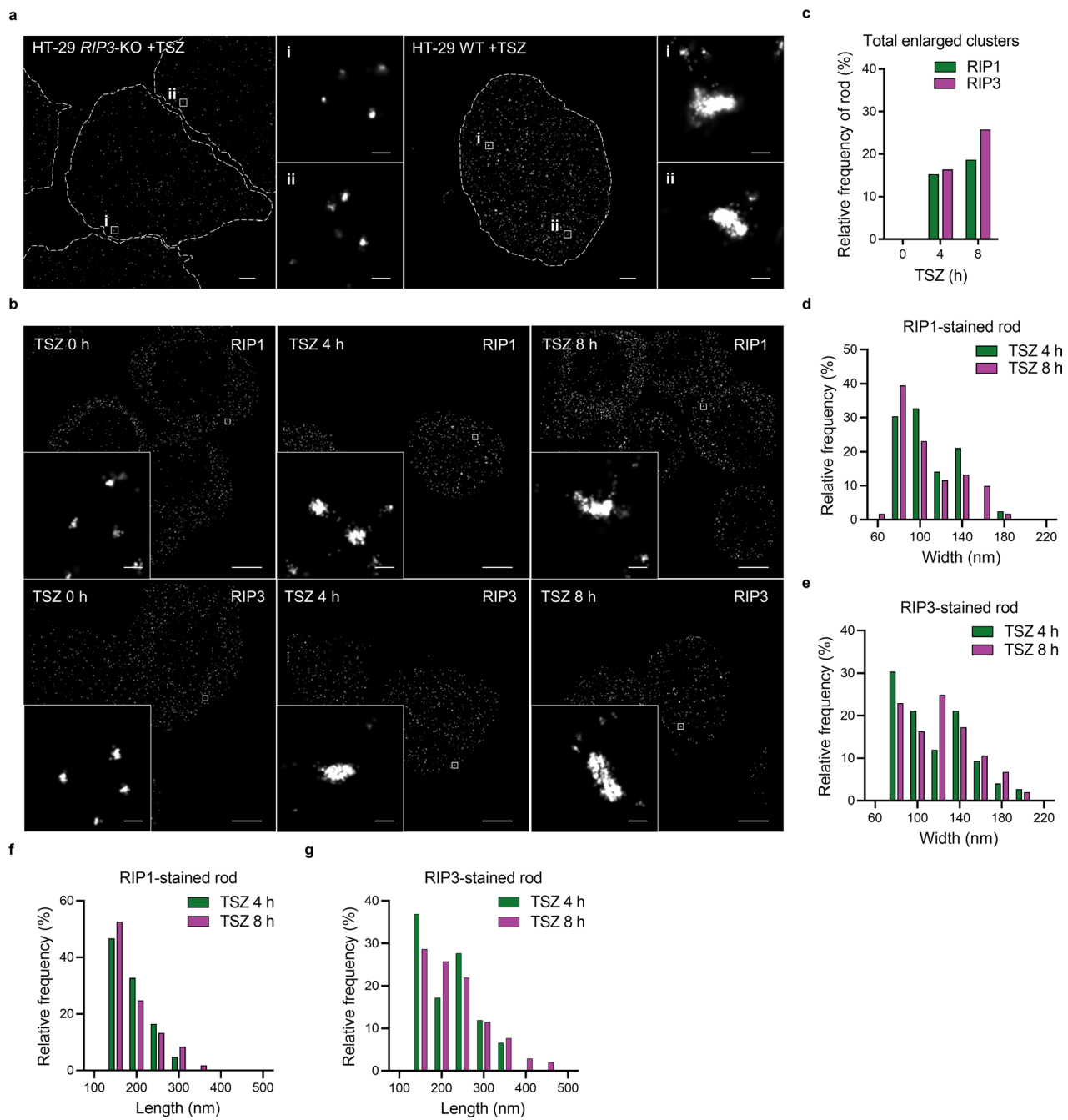
Reprints and permissions information is available at www.nature.com/reprints.



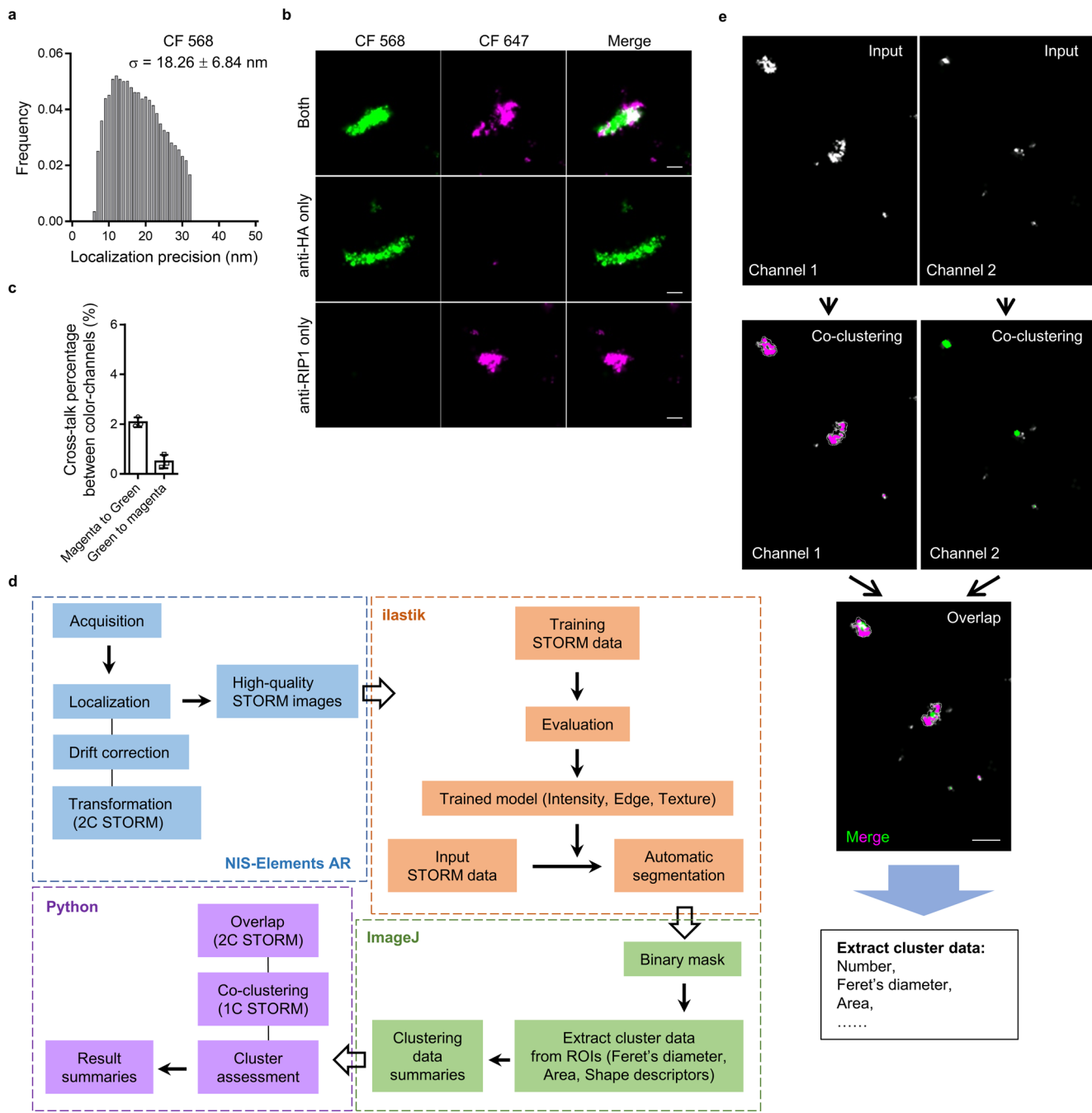
Extended Data Fig. 1 | Necrosome is visualized as diffraction-limited puncta growing in the process of cell necrosis. a, Confocal images of HA-RIP3 and MLKL-Flag-reconstituted MLKL-KO HeLa cells treated with DMSO or TSZ (T: TNF, 10 ng/ml; S: Smac mimetic (SM-164), 100 nM; Z: zVAD-fmk, 20 μ M), fixed and labeled for HA-RIP3 (green), RIP1 (purple) and MLKL-Flag (light blue). Red arrows in magnified images outlined by the white boxes emphasize the growing necrosome puncta. b-d, Intensity distribution of RIP1 (b, $n = 39, 232, 453$ for TSZ 0, 2, 4 h, respectively), RIP3 (c, $n = 59, 940, 1772$ for TSZ 0, 2, 4 h, respectively) or MLKL (d, $n = 11, 278, 735$ for TSZ 0, 2, 4 h, respectively) clusters detected in cells treated as in a. 'n' refers to the number of structures analyzed across two independent experiments. Box plots (b-d) show median and 25th to 75th percentiles, and whiskers indicate the minimum and maximum values. P values are determined by Kruskal-Wallis test with Dunn's multiple comparisons test. Scale bars, 10 μ m (original images) and 2 μ m (magnified images). Statistical source data are provided in Source Data Extended Data Fig. 1.



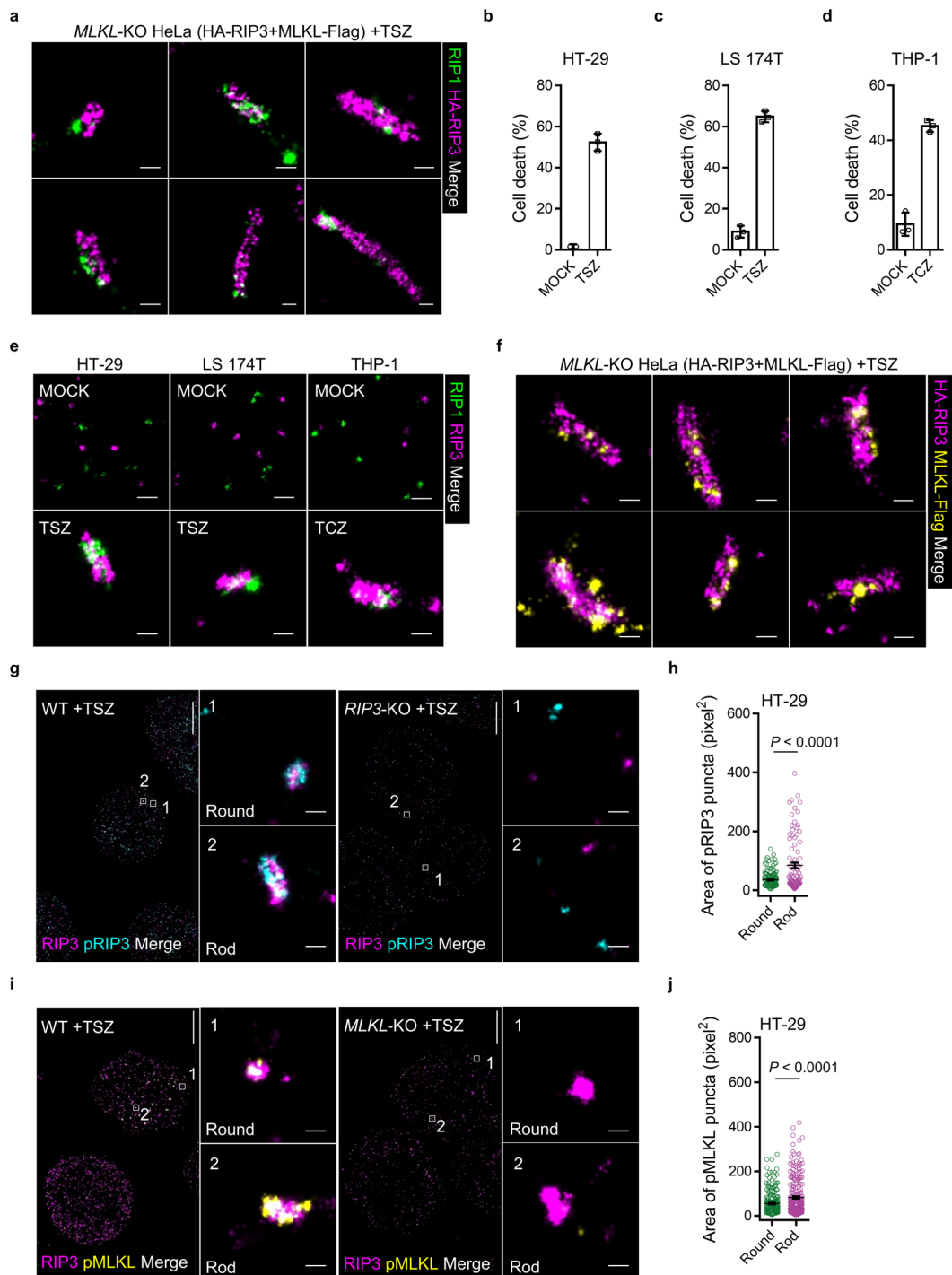
Extended Data Fig. 2 | Analysis of single-color STORM images. a, Representative histogram of localization precision of CF 647 calculated by LAMA algorithm³¹. b-e, Segmentation analysis of single-color STORM images (b). An example of RIP1 puncta (yellow) identified by machine learning-based algorithm (ilastik) in untreated HeLa cells expressing RIP3 is shown (c). The details of segmentation analysis are described in the Methods section. Area distribution (d) and ellipticity distribution (e) of RIP1 clusters were automatically quantified. Here, r value represents the effective diameter of the square with an equivalent area to the detected signals. The clusters with r value of more than 80 nm are TSZ-induced clusters and among them, those with an ellipticity of more than 2.00 are further regarded as rod-shaped structures. Scale bar, 100 nm. Statistical source data are provided in Source Data Extended Data Fig. 2.



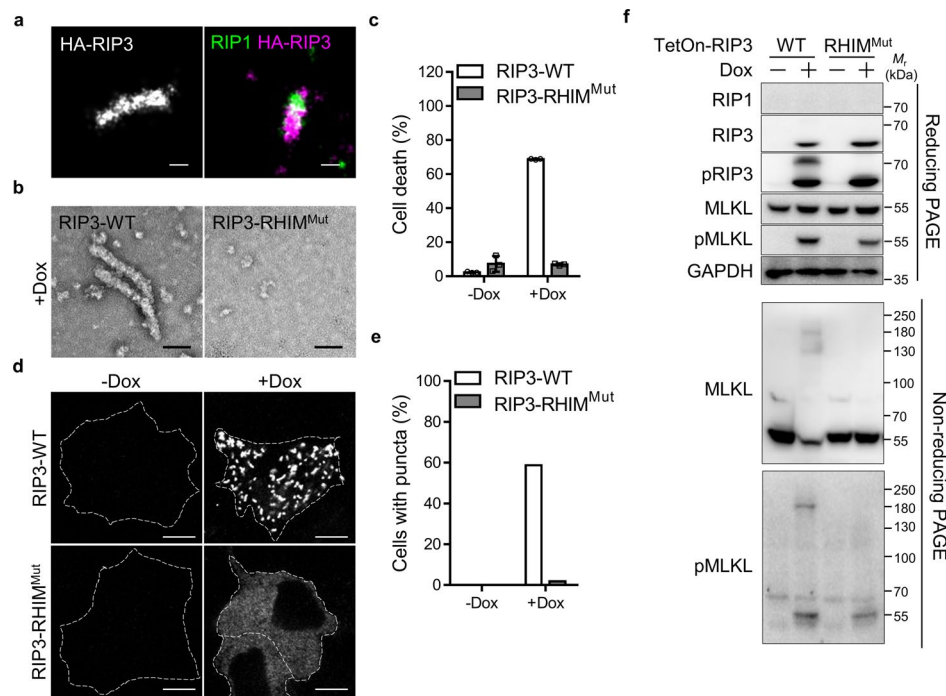
Extended Data Fig. 3 | Rod-shaped structure is a general feature of cellular necrosome. a, Single-color STORM images of endogenous RIP3 complexes revealed by using an anti-RIP3 antibody. Magnified images outlined by white boxes emphasize the rod-shaped RIP3 complexes only present in WT but not RIP3-deficient HT-29 cells treated with TSZ for 8 h. b, STORM images of RIP1 or RIP3 in HT-29 cells treated with TSZ (T: TNF, 10 ng/ml; S: Smac mimetic (SM-164), 100 nM; Z: zVAD-fmk, 20 μM) for indicated time. Magnified images are shown as inset figures, highlighting the RIP1 or RIP3 clusters during cell necroptosis. c, Percentage of rod-shaped structures detected by RIP1 or RIP3 staining in total enlarged clusters (RIP1, n=1, 277, 334 for TSZ 0, 4, 8 h, respectively; RIP3, n=8, 468, 409 for TSZ 0, 4, 8 h, respectively) by TSZ stimulation. The definitions of round- and rod-shaped structures are described in Extended Data Fig. 2d,e. d-g, Width (d) and length (f) distributions of RIP1 stained rods (n=43, 61 for TSZ 4, 8 h, respectively) or width (e) and length (g) distributions of RIP3 stained rods (n=76, 105 for TSZ 4, 8 h, respectively) in necroptotic HT-29 cells treated as in b. In c-g, 'n' refers to the number of structures analyzed across three independent experiments. Scale bars, 5 μm (original images in a and b) and 100 nm (magnified images in a and b). Statistical source data are provided in Source Data Extended Data Fig. 3.



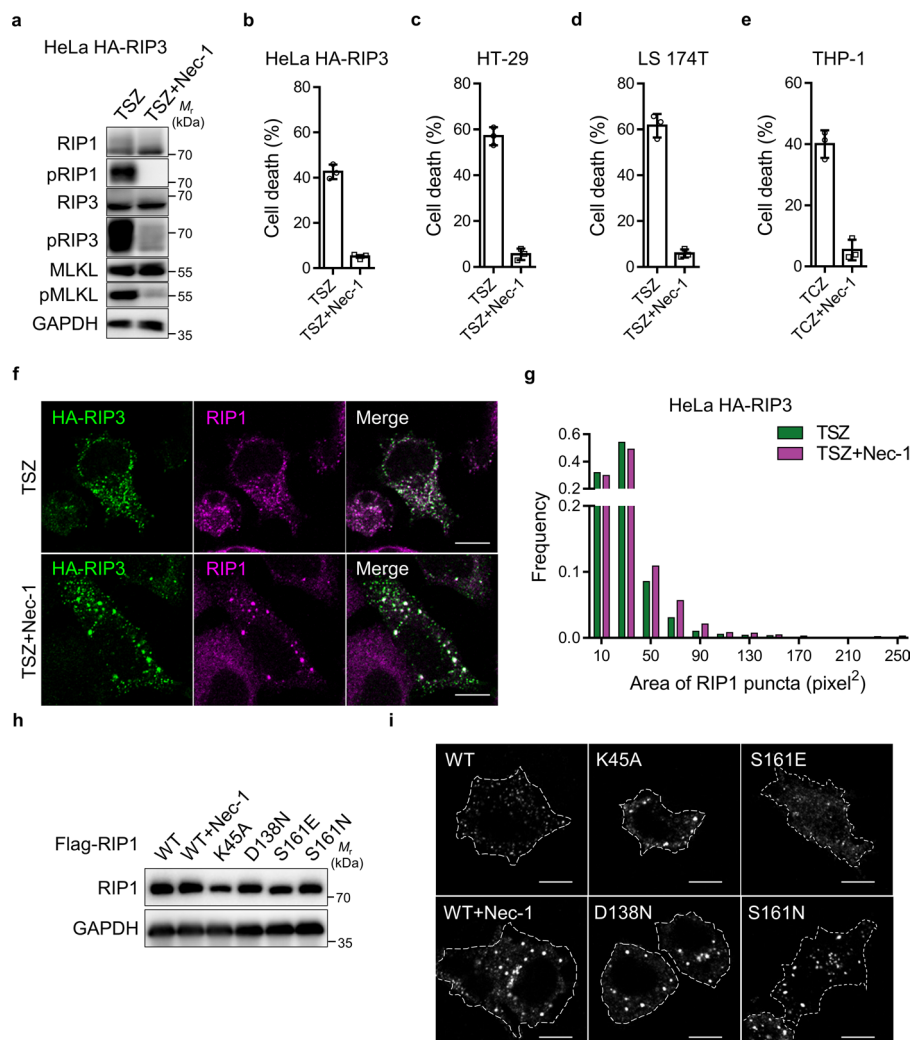
Extended Data Fig. 4 | Analysis of two-color STORM images. a, Representative histogram of localization precision of CF 568 calculated by LAMA algorithm³¹. b, Two-color STORM images of the RIP1-RIP3 necrosomes in HA-RIP3 expressing HeLa cells treated with TSZ, and labeled for RIP1 and RIP3 (top, “both”), only for RIP3 (middle, “anti-HA only”) or only for RIP1 (bottom, “anti-RIP1 only”). Green indicates mouse secondary antibody conjugated CF 568, and purple indicates rabbit secondary antibody conjugated CF 647. Data are representative of four independent experiments. c, Cross-talk percentages between the two STORM color-channels determined from single-color-labeled necrosome shown in b. Data are mean \pm SD of biological triplicates. d,e, Analysis workflow of two-color STORM images in this study (d). Clusters identified by ilastik in each channel were further assessed the possibility of co-clustering in a single channel or overlap between two channels. An example of cluster analysis of two-color STORM imaging is shown in e. The details of segmentation/overlap analysis of clusters are described in the Methods section. Scale bars, 200 nm (e) and 100 nm (b). Statistical source data are provided in Source Data Extended Data Fig. 4.



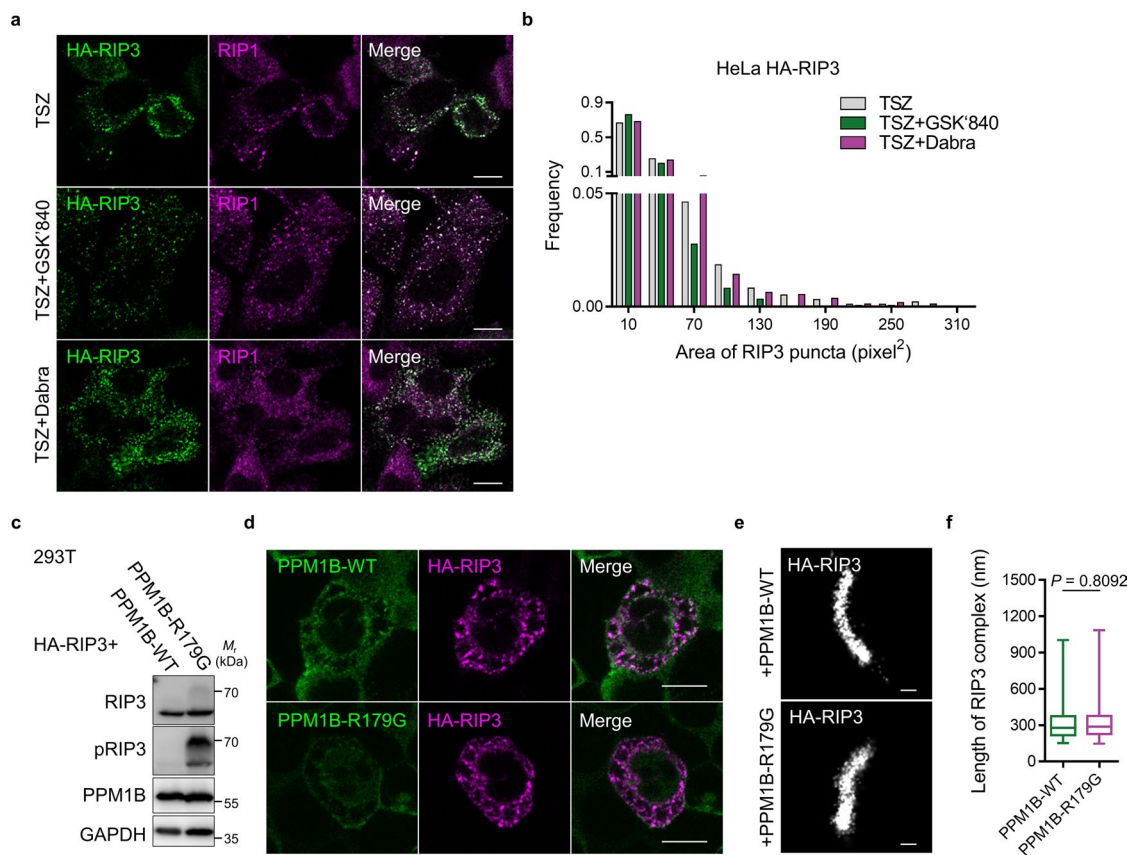
Extended Data Fig. 5 | Two-color STORM imaging of rod-shaped necrosomes. **a**, Two-color STORM of necrosomes showing the spatial localization of RIP1-RIP3 in HA-RIP3 and MLKL-Flag-expressing *MLKL-KO* HeLa cells treated with TSZ. **b-d**, Viability of HT-29 (**b**), LS 174 T (**c**) or THP-1 (**d**) cells treated as indicated. THP-1 cells were primed by 100 nM PMA. Data are represented as mean \pm SD of biological triplicates. **e**, Two-color STORM images of RIP1 and RIP3 clusters in cells from (**b-d**). **f**, Two-color STORM of necrosomes showing the spatial localization of RIP3-MLKL in HA-RIP3 and MLKL-Flag-expressing *MLKL-KO* HeLa cells treated with TSZ. **g-j**, Two-color STORM images showing the localizations of pRIP3 (**g**) or pMLKL (**i**) and RIP3 in WT and RIP3-deficient (**g**) or MLKL-deficient (**i**) HT-29 cells in the presence of TSZ. Area of pRIP3 ($n=163$, 90 structures analyzed across three independent experiments for Round or Rod, respectively, **h**) or pMLKL ($n=237$, 237 structures analyzed across three independent experiments for Round or Rod, respectively, **j**) puncta in round-/rod-shaped necrosome were calculated. STORM images are representative of three independent experiments. Data in **h** and **j** are mean \pm SEM. All P values are determined by two-tailed, unpaired t -test. Scale bars, 5 μ m (original images in **g** and **i**) and 100 nm (**a**, **e**, **f**) and magnified images in **g** and **i**). Statistical source data are provided in Source Data Extended Data Fig. 5.



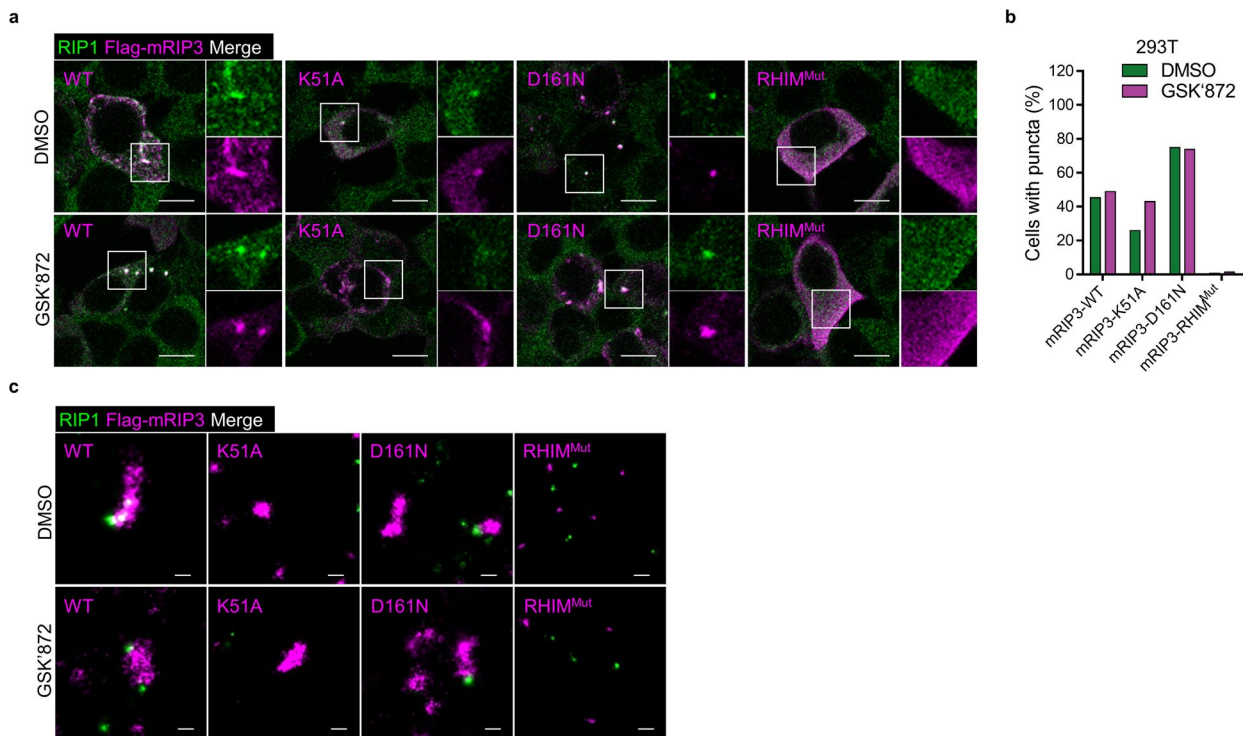
Extended Data Fig. 6 | RIP1 is dispensable for RIP3 rods formation by overexpressed RIP3 and RIP3 overexpression-induced necrosis. a, Single-color STORM image of RIP3 complex by Dox-induced RIP3 in RIP1-deficient HeLa cells (left) and two-color STORM image of TSZ-induced RIP1-RIP3 rod in HA-RIP3 expressing HeLa cells (right). b-f, Flag-RIP3-WT or Flag-RIP3-RHIM^{Mut} expression was induced in RIP1-deficient HeLa cells by addition of Dox. The RIP3-containing complex was immunoprecipitated with an anti-Flag antibody and visualized by using negative stain EM (b). Cell viability was measured based on quantitation of the ATP present (c). Data are represented as mean \pm SD of biological triplicates. Confocal images of RIP3 are shown (d) and the fraction of cells with RIP3 puncta were calculated (e). $n = 75\text{--}324$ cells pooled by two independent experiments. Cell lysates were collected and analyzed by immunoblotting for the indicated proteins under reducing or non-reducing conditions (f). Scale bars, 10 μm (d) and 100 nm (a and b). Unprocessed blots and statistical source data are provided in Source Data Extended Data Fig. 6.



Extended Data Fig. 7 | Disordered RIP1 complexes by non-phosphorylated RIP1. a, HA-RIP3-expressing HeLa cells were treated with TSZ or TSZ plus Nec-1. Cell lysates were collected and subjected to western blot analysis for the indicated proteins. b-e, Viability of HA-RIP3 expressing HeLa (b), HT-29 (c), LS 174 T (d) and THP-1 (e) cells treated as indicated. THP-1 cells were primed by 100 nM PMA. Data are represented as mean \pm SD of biological triplicates. f,g, Confocal images of RIP1 and RIP3 (f) and area distribution of RIP1 clusters (g, $n = 2015$ for TSZ and $n = 1131$ for TSZ + Nec-1) in cells treated as in b. 'n' refers to the number of structures analyzed across two independent experiments. h, Flag-RIP1 WT or mutants were overexpressed in *RIP1*-KO HeLa cells with or without Nec-1 for 24 h. Cell lysates were collected and subjected to western blot analysis for the indicated proteins. i, Confocal images of Flag-RIP1 WT or mutants in cells treated as in h. The experiment was performed twice with similar results. Scale bars, 10 μm . Unprocessed blots and statistical source data are provided in Source Data Extended Data Fig. 7.

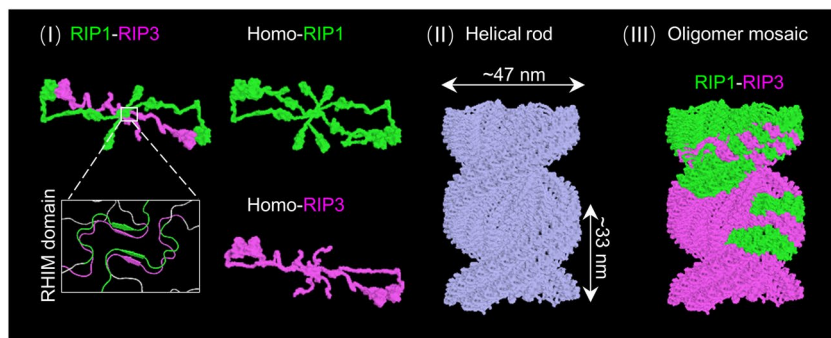


Extended Data Fig. 8 | Effect of RIP3 kinase inhibitors on the necrosome formation. a, Confocal images of the RIP1-RIP3 necrosomes in RIP3-expressing HeLa cells treated with TSZ or TSZ plus RIP3 kinase inhibitors (GSK'840 or Dabra). Purple indicates RIP1 and green is RIP3. b, Area histogram of RIP3 puncta in cells from a. $n = 973-3524$ clusters from 10 fields. c-f, Flag-RIP3 was co-overexpressed with PPM1B WT or its inactive form (R179G) in HEK293T cells. Cell lysates were collected and subjected to western blot analysis for the indicated proteins. Data are representative of three independent experiments (c). Representative confocal images of RIP3 and PPM1B-WT or PPM1B-R179G from two independent experiments (d). STORM images (e) and length distribution (f) of RIP3 rods in the presence of PPM1B WT or R179G mutant ($n = 699$ for WT and $n = 589$ for R179G). 'n' refers to the number of structures analyzed across two independent experiments. Box plots show median and 25th to 75th percentiles, and whiskers indicate the minimum and maximum values. *P* values are determined by two-tailed, unpaired *t*-test. Scale bars, 10 μ m (a and d) and 100 nm (e). Unprocessed blots and statistical source data are provided in Source Data Extended Data Fig. 8.

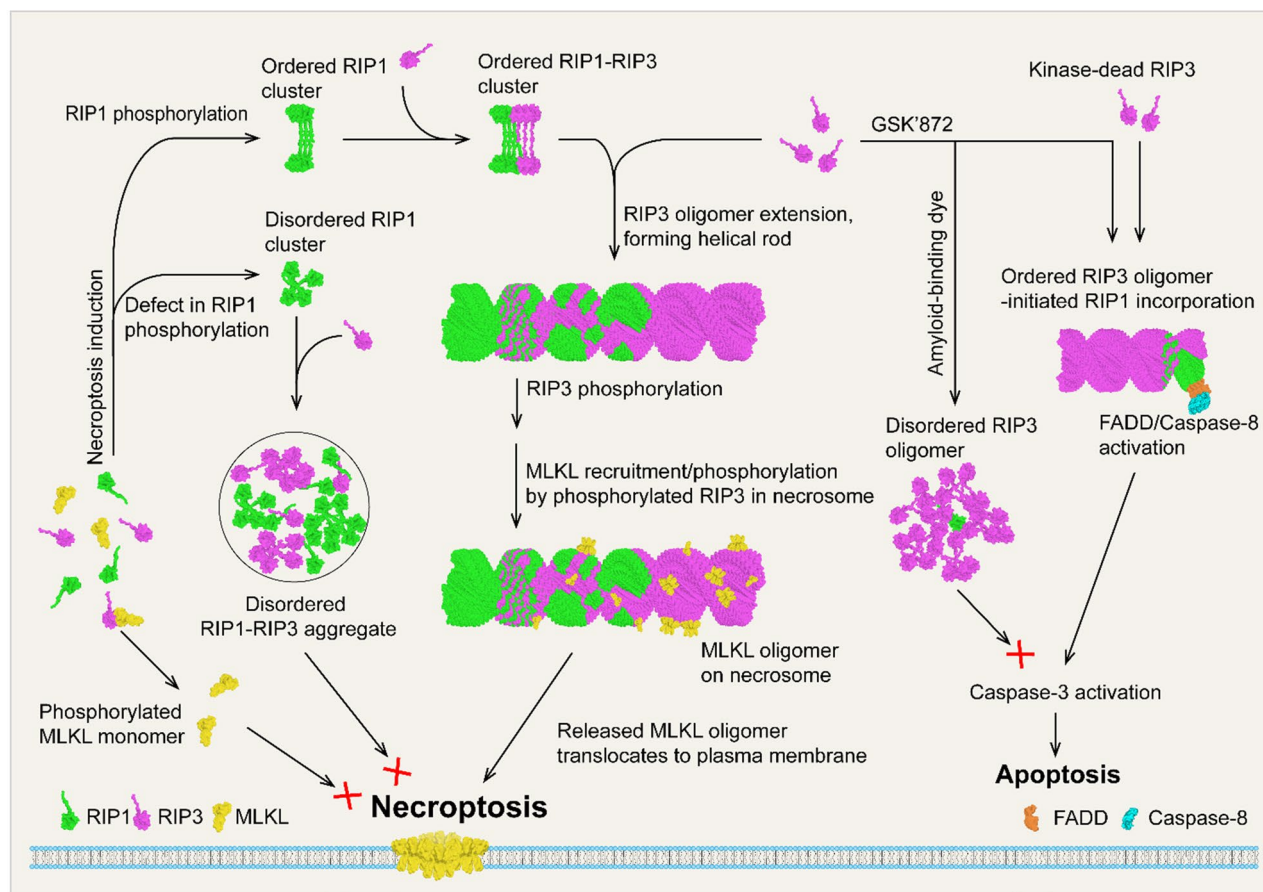


Extended Data Fig. 9 | The effects of expression of mRIP3 WT or mutants in HEK293T cells. a-c, Flag-mRIP3 WT or mutants (K51A, D161N, or RHIM^{Mut}) were expressed in HEK293T cells with or without 5 μ M GSK872. Confocal (a) and STORM (c) images of RIP1-RIP3 complexes are shown. The fraction of cells with RIP3 puncta is calculated (b). $n=97-156$ cells pooled by two independent experiments. Data in c are representative of three independent experiments. Scale bars, 10 μ m (a) and 100 nm (c). Statistical source data are provided in Source Data Extended Data Fig. 9.

a



b



Extended Data Fig. 10 | Model of the assembly and function of mosaic RIP1-RIP3 rods. a, A hypothetical model of RIP1-RIP3 mosaics: (I) Bidirectional β sheets resulted from RHIM-dependent RIP1/RIP3 homo- or hetero-interactions; (II) The β sheets further form helical necrosome rods with about 47 nm in width and 33 nm in pitch length; (III) RIP1/RIP3 homo-oligomers distribute heterogeneously in the rod-shaped necrosome, exhibiting a mosaic pattern. b, Upon necroptosis stimuli, RIP1 is autophosphorylated and this modification retains RIP1 assembly in a proper manner. Ordered RIP1 interaction initiates ordered recruitment of downstream RIP3, leading to the formation of helical rod-shaped necrosomes. Necrosomal RIP1- and RIP3-homo-oligomers distribute as a mosaic pattern, and RIP3 oligomers with sizes equal to or more than tetramer license phosphorylated MLKL to oligomerize for necroptosis. RHIM domain-mediated interaction rather than RIP3 autophosphorylation/MLKL recruitment is indispensable for the formation of rod-shaped necrosomes. In addition, the mosaic RIP1-RIP3 rods are essential for apoptosis by recruiting FADD/Caspase-8 when RIP3 kinase activity was eliminated by GSK872 or by kinase-dead mutations. Disrupting the ordered RIP1-RIP3 rod-shaped structures could impair the recruitment/activation of downstream molecules. Thus, the ordered RIP1-RIP3 mosaic rod functions as a bidirectional module for the signaling of necroptosis and apoptosis under certain conditions.

Reporting Summary

Nature Portfolio wishes to improve the reproducibility of the work that we publish. This form provides structure for consistency and transparency in reporting. For further information on Nature Portfolio policies, see our [Editorial Policies](#) and the [Editorial Policy Checklist](#).

Statistics

For all statistical analyses, confirm that the following items are present in the figure legend, table legend, main text, or Methods section.

n/a Confirmed

- The exact sample size (n) for each experimental group/condition, given as a discrete number and unit of measurement
- A statement on whether measurements were taken from distinct samples or whether the same sample was measured repeatedly
- The statistical test(s) used AND whether they are one- or two-sided
Only common tests should be described solely by name; describe more complex techniques in the Methods section.
- A description of all covariates tested
- A description of any assumptions or corrections, such as tests of normality and adjustment for multiple comparisons
- A full description of the statistical parameters including central tendency (e.g. means) or other basic estimates (e.g. regression coefficient) AND variation (e.g. standard deviation) or associated estimates of uncertainty (e.g. confidence intervals)
- For null hypothesis testing, the test statistic (e.g. F , t , r) with confidence intervals, effect sizes, degrees of freedom and P value noted
Give P values as exact values whenever suitable.
- For Bayesian analysis, information on the choice of priors and Markov chain Monte Carlo settings
- For hierarchical and complex designs, identification of the appropriate level for tests and full reporting of outcomes
- Estimates of effect sizes (e.g. Cohen's d , Pearson's r), indicating how they were calculated

Our web collection on [statistics for biologists](#) contains articles on many of the points above.

Software and code

Policy information about [availability of computer code](#)

Data collection

All the instruments used are commercially available and were controlled using the software by the manufacturer.
 ZEN 2012 Black acquisition software v. 8.0.5.273 (Zeiss, LSM780 confocal microscopy)
 NIS-Elements AR software v. 4.50.00 (Nikon, N-STORM super-resolution microscopy)
 Hitachi TEM system control software (Hitachi, HT 7800 transmission electron microscopy)
 JPK SPM software v. 7.0.113 (Bruke, NanoWizard 4 XP NanoScience atomic force microscopy)
 AI 680 software (GE Healthcare, Amersham Imager 680)
 Omega software v. 5.1.2600.5512 (BMG Labtech, POLARstar Omega)
 CellQuest Pro software v. 6.0 (BD, FACSCalibur Flow Cytometer)

Data analysis

NIS-Elements AR with N-STORM module v. 4.50.00 (Nikon, for reconstruction and visualization of super-resolution images)
 Fiji/Image J v. 1.53f51 (for data visualization and statistics)
 Excel 2016 (Microsoft, for image analysis data management)
 Ilastik v. 1.3.3post3 (for cluster segmentation of STORM images)
 JPK SPM v. 7.0.113 (Bruke, for visualization of AFM images)
 Pymol v. 2.4 (for visualization of modeled structures)
 Prism v. 6.02 (GraphPad, for data visualization and statistics)
 Other software used include Visual Studio Code (v. 1.62.3), python (v. 3.8.5). Python packages used OpenCV-python (v. 4.5.3.56), NumPy (v. 1.19.5), Pandas (v. 1.1.3). Custom code written for the cluster analysis of STORM image has been deposited to Github (<https://github.com/xchenxmu/STORMing-the-necrosome.git>)

For manuscripts utilizing custom algorithms or software that are central to the research but not yet described in published literature, software must be made available to editors and reviewers. We strongly encourage code deposition in a community repository (e.g. GitHub). See the Nature Portfolio [guidelines for submitting code & software](#) for further information.

Data

Policy information about [availability of data](#)

All manuscripts must include a [data availability statement](#). This statement should provide the following information, where applicable:

- Accession codes, unique identifiers, or web links for publicly available datasets
- A description of any restrictions on data availability
- For clinical datasets or third party data, please ensure that the statement adheres to our [policy](#)

Numerical source data giving rise to graphical representations and unprocessed images of blots are shown in Source Data Figures. Detailed experimental procedures and additional data supporting the findings of this study are available from the corresponding author on reasonable request. All Python scripts and Fiji macros for STORM image analysis are available in the online repository Github (<https://github.com/xchenxmu/STORMing-the-necrosome.git>). The published structures of RIP1-RIP3 hetero-amyloid core (PDB: 5V7Z), RIP1 kinase domain (PDB: 4NEU), RIP1 death domain (PDB: 6AC5) and RIP3 kinase domain (PDB: 4M66) were accessible in the Protein Data Bank (PDB, <https://www.rcsb.org/>) with related IDs.

Field-specific reporting

Please select the one below that is the best fit for your research. If you are not sure, read the appropriate sections before making your selection.

- Life sciences Behavioural & social sciences Ecological, evolutionary & environmental sciences

For a reference copy of the document with all sections, see nature.com/documents/nr-reporting-summary-flat.pdf

Life sciences study design

All studies must disclose on these points even when the disclosure is negative.

Sample size	No statistical methods were used to predetermine sample size, as this study did not include animal models or human participants. Sample size was determined based on standards in the field (Zhou et al., <i>Science</i> , 2019; Simoncelli et al., <i>Cell Reports</i> , 2020; Xu et al., <i>Nature Communications</i> , 2020) and experimental experience to obtain statistical significance and reproducibility.
Data exclusions	No data were excluded, except in the case of obvious technical error.
Replication	All experimental findings were reliably reproduced in at least two independent experiments as indicated in the figure legends. All attempts of replication were successful.
Randomization	No randomization was done, because this study does not involve animals or human participants. Samples were organized into groups based on treatments (e.g. RIP3 wild-type compared to its mutants; experimental time-points). Appropriate controls were included in all experiments.
Blinding	For microscopy data collection, researchers were not blinded to samples but fields of view were chosen on a random basis, preventing potentially biased selection for desired phenotypes.

Reporting for specific materials, systems and methods

We require information from authors about some types of materials, experimental systems and methods used in many studies. Here, indicate whether each material, system or method listed is relevant to your study. If you are not sure if a list item applies to your research, read the appropriate section before selecting a response.

Materials & experimental systems

n/a	Involved in the study
<input type="checkbox"/>	<input checked="" type="checkbox"/> Antibodies
<input type="checkbox"/>	<input checked="" type="checkbox"/> Eukaryotic cell lines
<input checked="" type="checkbox"/>	<input type="checkbox"/> Palaeontology and archaeology
<input checked="" type="checkbox"/>	<input type="checkbox"/> Animals and other organisms
<input checked="" type="checkbox"/>	<input type="checkbox"/> Human research participants
<input checked="" type="checkbox"/>	<input type="checkbox"/> Clinical data
<input checked="" type="checkbox"/>	<input type="checkbox"/> Dual use research of concern

Methods

n/a	Involved in the study
<input checked="" type="checkbox"/>	<input type="checkbox"/> ChIP-seq
<input type="checkbox"/>	<input checked="" type="checkbox"/> Flow cytometry
<input checked="" type="checkbox"/>	<input type="checkbox"/> MRI-based neuroimaging

Antibodies

Antibodies used

Antibody, Supplier, Cat. number, Lot. number, Technique, Concentration
 RIP1, Cell Signaling, 3493, N/A, 1:150 for IF, 1:1,000 for WB
 phospho Ser166 RIP1, Cell Signaling, 65746, N/A, 1:1,000 for WB
 RIP3, Santa Cruz, sc-374639, L1817, 1:150 for IF

RIP3, Cell Signaling, 13526, N/A, 1:1,000 for WB
 phospho Ser227 RIP3, Abcam, ab209384, GR3283115-3, 1:1,000 for WB; 1:500 for IF
 MLKL, Abcam, ab184718, GR3211572-16, 1:1,000 for WB
 phospho Ser358 MLKL, Abcam, ab187091, GR212667-41, 1:1,000 for WB; 1:200 for IF
 Caspse-3, Cell Signaling, 9662, N/A, 1:1,000 for WB
 PPM1B, Abcam, ab70804, 1:1,000 for WB
 HA, Santa Cruz, sc-7392, F119, 1:200 for IF, 1:1,000 for WB
 HA, Cell Signaling, 3724, N/A, 1:200 for IF, 1:1,000 for WB
 Flag, Cell Signaling, 8146, N/A, 1:200 for IF, 1:1,000 for WB
 Flag, Biolegend, 637301, B219947, 1:200 for IF
 GAPDH, ABclonal, AC002, 1:5,000 for WB
 Goat anti-rabbit Alexa Fluor 488, Thermo Fisher Scientific, A11034, 2069632, 1:1,000 for IF
 Goat anti-mouse Alexa Fluor 568, Thermo Fisher Scientific, A11004, 1906485, 1:1,000 for IF
 Goat anti-rat Alexa Fluor 647, Thermo Fisher Scientific, A21247, 2219256, 1:1,000 for IF
 Goat anti-rabbit CF 568, Biotium, 20801, 17C0126, 1:500 for IF
 Goat anti-mouse CF 568, Biotium, 20800, 17C0126, 1:500 for IF
 Goat anti-rabbit CF 647, Biotium, 20809, 17C0322, 1:500 for IF
 Goat anti-mouse CF 647, Biotium, 20808, 17C1006, 1:500 for IF

Validation

Antibodies for western blotting and immunofluorescence were validated by manufacturer:
 RIP1 (Cell signaling, 3493):<https://www.cellsignal.com/products/primary-antibodies/rip-d94c12-xp-rabbit-mab/3493>
 phospho Ser166 RIP1 (Cell Signaling, 65746):<https://www.cellsignal.com/products/primary-antibodies/phospho-rip-ser166-d1l3s-rabbit-mab/65746>
 RIP3 (Santa Cruz, sc-374639):<https://www.scbt.com/p/rip3-antibody-b-2?requestFrom=search>
 RIP3 (Cell Signaling, 13526):<https://www.cellsignal.com/products/primary-antibodies/rip3-e1z1d-rabbit-mab/13526>
 phospho Ser227 RIP3 (Abcam, ab209384):<https://www.abcam.com/nav/primary-antibodies/rabbit-monoclonal-antibodies/rip3-phospho-s227-antibody-epr9627-ab209384.html>
 MLKL (Abcam, ab184718):<https://www.abcam.com/mlkl-antibody-epr17514-ab184718.html>
 phospho Ser358 MLKL (Abcam, ab187091):<https://www.abcam.com/mlkl-phospho-s358-antibody-epr9514-ab187091.html>
 Caspse-3 (Cell Signaling, 9662):<https://www.cellsignal.com/products/primary-antibodies/caspase-3-antibody/9662>
 PPM1B (Abcam, ab70804):<https://www.abcam.com/ppm1b-antibody-ab70804.html>
 HA (Santa Cruz, sc-7392):<https://www.scbt.com/zh/p/ha-probe-antibody-f-7?requestFrom=search>
 HA (Cell Signaling, 3724):<https://www.cellsignal.com/products/primary-antibodies/ha-tag-c29f4-rabbit-mab/3724>
 Flag (Cell Signaling, 8146):<https://www.cellsignal.com/products/primary-antibodies/dykdddk-tag-9a3-mouse-mab-binds-to-same-epitope-as-sigma-s-anti-flag-m2-antibody/8146>
 Flag (Biolegend, 637301):<https://www.biolegend.com/en-us/products/purified-anti-dykdddk-tag-antibody-4905>
 GAPDH (ABclonal, AC002):<https://abclonal.com.cn/catalog/AC002>
 Goat anti-rabbit Alexa Fluor 488 (Thermo Fisher Scientific, A11034):<https://www.thermofisher.cn/cn/en/antibody/product/Goat-anti-Rabbit-IgG-H-L-Highly-Cross-Adsorbed-Secondary-Antibody-Polyclonal/A-11034>
 Goat anti-mouse Alexa Fluor 568 (Thermo Fisher Scientific, A11004):<https://www.thermofisher.cn/cn/en/antibody/product/Goat-anti-Mouse-IgG-H-L-Cross-Adsorbed-Secondary-Antibody-Polyclonal/A-11004>
 Goat anti-rat Alexa Fluor 647 (Thermo Fisher Scientific, A21247):<https://www.thermofisher.cn/cn/en/antibody/product/Goat-anti-Rat-IgG-H-L-Cross-Adsorbed-Secondary-Antibody-Polyclonal/A-21247>
 Goat anti-rabbit CF 568 (Biotium, 20801):<https://biotium.com/product/goat-anti-rabbit-igg-hl-highly-cross-absorbed-cf-dye-storm/>
 Goat anti-mouse CF 568 (Biotium, 20800):<https://biotium.com/product/goat-anti-mouse-igg-hl-highly-cross-absorbed-cf-dye-storm/>
 Goat anti-rabbit CF 647 (Biotium, 20809):<https://biotium.com/product/goat-anti-rabbit-igg-hl-highly-cross-absorbed-cf-dye-storm/>
 Goat anti-mouse CF 647 (Biotium, 20808):<https://biotium.com/product/goat-anti-mouse-igg-hl-highly-cross-absorbed-cf-dye-storm/>

Further validation of antibodies is provided in this study using positive and negative controls (knockouts, induction treatments or specific site phosphorylation defect mutation) for the following antibodies: RIP1 (Cell signaling, 3493; Fig. 4d, ED Fig. 6f), phospho-Ser166-RIP1 (Cell Signaling, 65746; Fig. 6b, l, ED Fig. 7a), RIP3 (Cell Signaling, 13526; Fig. 3g, 4d, ED Fig. 6f), RIP3 (Santa Cruz, sc-374639; ED Fig. 3a, 5g), phospho-S227-RIP3 (Abcam, ab209384; Fig. 2k, m, 4d, 6b, l, ED Fig. 5g, 6f, 7a, 8c), MLKL (Abcam, ab184718; Fig. 3g, 4d), and phospho-S358-MLKL (Abcam, ab187091; Fig. 3g, 4d, 6b, l, ED Fig. 5i, 6f, 7a).

Eukaryotic cell lines

Policy information about [cell lines](#)

Cell line source(s)

Cell lines used were listed as name, source and identifier.
 HEK293T, ATCC, CRL-11268
 HeLa, ATCC, CCL-2
 HT-29, ATCC, HTB-38
 L929, ATCC, CCL-1
 THP-1, ATCC, TIB-202
 LS 174T, Dr. Sudan He, Suzhou Institute of Systems Medicine, N/A
 L929-RIP3-KO, Chen et al. J Biol Chem, 2013, N/A
 HT-29-RIP3-KO, Huang et al. Cell Host Microbe, 2015, N/A
 HeLa-RIP1-KO, this paper, N/A
 HeLa-MLKL-KO, this paper, N/A
 HT-29-MLKL-KO, this paper, N/A

Authentication

No additional authentication was performed.

Mycoplasma contamination

All cell lines were routinely tested to be free of mycoplasma contamination.

Commonly misidentified lines
(See [ICLAC](#) register)

No cell lines used in this study were found in the database of commonly misidentified cell lines that is maintained by ICLAC and NCBI biosample.

Flow Cytometry

Plots

Confirm that:

- The axis labels state the marker and fluorochrome used (e.g. CD4-FITC).
- The axis scales are clearly visible. Include numbers along axes only for bottom left plot of group (a 'group' is an analysis of identical markers).
- All plots are contour plots with outliers or pseudocolor plots.
- A numerical value for number of cells or percentage (with statistics) is provided.

Methodology

Sample preparation

Cells were cultured in 12-well or 6-well plates, trypsin-digested and stained with Propidium iodide (PI) before flow cytometry analysis.

Instrument

BD FACS calibur

Software

BD CellQuest Pro v. 6.0

Cell population abundance

10 000 cells per sample were analysed. All cells apart from FSC/SSC scatter dot blot based debris and aggregates were analyzed.

Gating strategy

For cell survival analysis by PI staining, the instrument settings were set as: Detector: FSC, Voltage: E-1, AmpGain: 5.50, Mode: Lin; Detector: SSC, Volgate: 350, AmpGain: 1.00, Mode: Lin; Detector: FL3, Voltage: 400, AmpGain: 1.00, Mode: Log; Cells with FSC between 8×10^5 to 3×10^6 and FL3 less than 10^2 were defined as PI-negative living cells.

- Tick this box to confirm that a figure exemplifying the gating strategy is provided in the Supplementary Information.